JGR Atmospheres

RESEARCH ARTICLE
10.1029/2019JD032210

Dust Deposited on Snow Cover in the San Juan Mountains, Colorado, 2011–2016: Compositional Variability Bearing on Snow-Melt Effects

Richard L. Reynolds[1,2], Harland L. Goldstein[1], Bruce M. Moskowitz[2], Raymond F. Kokaly[3], Seth M. Munson[4], Peat Solheid[2], George N. Breit[3], Corey R. Lawrence[1], and Jeff Derry[5]

[1]U.S. Geological Survey, Geosciences and Environmental Change Science Center, Denver, CO, USA, [2]Institute for Rock Magnetism, Department of Earth and Environmental Sciences, University of Minnesota, Minneapolis, MN, USA, [3]U.S. Geological Survey, Geology, Geophysics, Geochemistry Science Center, Denver, CO, USA, [4]U.S. Geological Survey, Southwest Biological Science Center, Flagstaff, AZ, USA, [5]Center for Snow and Avalanche Studies, Silverton, CO, USA

Abstract Light-absorbing particles in atmospheric dust deposited on snow cover (dust-on-snow, DOS) diminish albedo and accelerate the timing and rate of snow melt. Identification of these particles and their effects is relevant to snow-radiation modeling and water-resource management. Laboratory-measured reflectance of DOS samples from the San Juan Mountains (USA) were compared with DOS mass loading, particle sizes, iron mineralogy, carbonaceous matter type and content, and chemical compositions. Samples were collected each spring for water years 2011–2016, when individual dust layers had merged into one (all layers merged) at the snow surface. Average reflectance values of the six samples were 0.2153 (sd, 0.0331) across the visible wavelength region (0.4–0.7 μm) and 0.3570 (sd, 0.0498) over the full-measurement range (0.4–2.50 μm). Reflectance values correlated inversely to concentrations of ferric oxide, organic carbon (1.4–10 wt.%), magnetite (0.05–0.13 wt.%), and silt ($PM_{63\text{-}3.9}$; median grain sizes averaged 21.4 μm) but lacked correspondence to total iron and PM_{10} contents. Measurements of reflectance and Mössbauer spectra and magnetic properties indicated that microcrystalline hematite and nano-size goethite were primarily responsible for diminished visible reflectance. Positive correlations between organic carbon and metals attributed to fossil-fuel combustion, with observations from electron microscopy, indicated that some carbonaceous matter occurred as black carbon. Magnetite was a surrogate for related light-absorbing minerals, dark rock particles, and contaminants. Similar analyses of DOS from other areas would help evaluate the influences of varied dust sources, wind-storm patterns, and anthropogenic inputs on snow melt and water resources in and beyond the Colorado River Basin.

Plain Language Summary Melted snow from mountains is a critical source of water for people and agriculture downstream, and the rate and timing of snow melt are important factors for water management. Along with air temperature, certain mineral and carbon-rich particles deposited as atmospheric dust on snow cover greatly affect snow melt because they absorb sunlight to warm snow. To understand better how snow melts, we identified these kinds of heat-absorbing particles in end-of-melt season, dark dust layers spanning 6 years (2011–2016) in the San Juan Mountains in the upper Colorado River Basin (USA). Melted snow from this basin is the major water source for 44 million people in the arid American Southwest. We found that three types of dust particles contributed most to heat absorption on snow surfaces: iron oxide minerals, dark rock fragments, and soot. The minerals and rock fragments originated in dust storms in deserts adjacent to the mountains, whereas the soot, which was associated with metals, was produced during fossil-fuel combustion likely from many widespread industrial activities. Similar analyses of dust-on-snow from other areas would help evaluate the influences of varied dust sources, wind-storm patterns, and anthropogenic inputs on snow melt in and beyond the Colorado River Basin.

Key Points:
- We characterized light-absorbing particles (LAPs) in atmospheric dust deposited on snow cover, San Juan Mountains, Colorado, 2011–2016
- The primary LAPs were ferric oxide minerals and dark rock particles mostly from dust storms, and black-carbon from industrial sources
- The results are relevant to snow-radiation modeling and water-resource management in the Colorado River Basin

Supporting Information:
- Supporting Information S1
- Table S8
- Table S10

Correspondence to:
R. L. Reynolds and H. L. Goldstein,
rreynolds@usgs.gov;
hgoldstein@usgs.gov

Citation:
Reynolds, R. L., Goldstein, H. L., Moskowitz, B. M., Kokaly, R. F., Munson, S. M., Solheid, P., et al. (2020). Dust deposited on snow cover in the San Juan Mountains, Colorado, 2011–2016: Compositional variability bearing on snow-melt effects. *Journal of Geophysical Research: Atmospheres*, *125*, e2019JD032210. https://doi.org/10.1029/2019JD032210

Received 7 DEC 2019
Accepted 24 FEB 2020
Accepted article online 10 MAR 2020

1. Introduction

Atmospheric dust consisting of mineral particles and other airborne particulate matter, such as certain forms of carbon, can have important effects on environments and people across the globe (e.g., Derbyshire, 2007; Field et al., 2009; Gassó et al., 2010; Goudie & Middleton, 2006; Jickells et al., 2005; Knippertz & Stuut, 2014; Lawrence et al., 2013; Maher et al., 2010; Mahowald et al., 2010; Shao

et al., 2011). As one such effect, dust can strongly influence the timing and rate of snow melt when it is deposited to snow surfaces (Deems et al., 2013; Landry et al., 2014; Painter et al., 2007, 2010 ; Painter, Bryant, & Skies, 2012; Painter, Skiles et al., 2012; Painter et al., 2018; Skiles et al., 2012, 2015, 2017; Skiles & Painter, 2016, 2017, 2018; Warren & Wiscombe, 1980; Wiscombe & Warren, 1980). This effect is a special concern in areas where downstream water users and managers depend on water delivery from mountains during the spring and summer melt season. The need for reliably available water from snow melt is especially acute in drylands downslope from mountain ranges, such as the southwestern United States (e.g., Udall, 2013). In this region, most water in the Colorado River and its contributing basins derives from melted snow principally from the central Rocky Mountains of Colorado. About 44 million inhabitants in seven southwestern states and Mexico, along with their associated activities, use water provided by the Colorado River Basin. Rapid and early snow melt has additional effects on montane ecosystems when ground is exposed earlier than during the prior ca. 150 years (see Neff et al., 2008) with consequences for a host of montane and downstream phenological responses and a longer season of soil-moisture loss through evapotranspiration (e.g., Steltzer et al., 2009).

Numerous studies have addressed the role of black carbon to promote melting of snow and ice (e.g., Bond et al., 2013; Bond & Bergstrom, 2006; Dang & Hegg, 2014; Doherty et al., 2014; Flanner et al., 2007, 2009, 2012; Gieré & Querol, 2010; Hadley & Kirschstetter, 2012; Qian et al., 2015; Ramanathan et al., 2007; Ramanathan & Carmichael, 2008; Wu et al., 2018). Moreover, several investigations have examined the combined effects of dust and black carbon on snow and ice melt in middle-latitude settings of North America (Hadley et al., 2010; Nagorski et al., 2019; Oaida et al., 2015), as well as Asia (Himalayas, Tibet, North China) and Europe (Alps) (Dang et al., 2017; Di Mauro et al., 2019; Ginot et al., 2014; Kaspari et al., 2014; Thind et al., 2019; Zhang et al., 2017, 2018; Zhao et al., 2014). In contrast, few studies have considered specific minerals in dust for their potential heat-absorbing effects on melting of snow cover (Axson et al., 2016; Kaspari et al., 2014; Lawrence et al., 2010; Reynolds, Goldstein et al., 2014).

In this study, we sought to understand particulate compositions in dust layers in the middle-latitude (37.3–38.2°N.) San Juan Mountains (SJM; maximum elevation, 4,360 m above sea level) of southwest Colorado, USA (Figure 1). The emphasis here is on the ferric iron oxide minerals (Fe_2O_3, hematite and α-FeOOH, goethite) because they strongly absorb solar radiation (Alfaro et al., 2004; Derimian et al., 2008; Engelbrecht et al., 2016; Gassó et al., 2010; Kaufman et al., 2001; Lafon et al., 2004, 2006; Moosmüller et al., 2012; Redmond et al., 2010; Sokolik et al., 2001; Sokolik & Toon, 1999; Zhang et al., 2015). We anticipated their presence from the colors of observed airborne and deposited dust in the SJM commonly comprising red, orange, and gray-brown hues. In addition, our on-going investigations of regional dust sources in the American Southwest confirm the common presence of ferric iron oxide minerals in dust-source sediments. Moreover, our investigations have pointed to the potential albedo effects of other heat-absorbing particles as revealed by the presence of ferrous-ferric iron oxide (e.g., Fe_3O_4, magnetite) in some DOS and source-area samples (Moskowitz et al., 2016; Reynolds, Goldstein et al., 2014). We also consider here possible roles of carbonaceous matter in albedo reduction, even though our dust-collection site is remote from major sources of black carbon, such as industrial areas, sites of fossil-fuel combustion for energy, and heavily used transportation corridors. Snow texture and consequently snow albedo can be affected by factors other than radiative forcing (RF) by particulates, such as by various controls on snow metamorphism (Hansen & Nazarenko, 2004; Painter et al., 2007; Painter, Skiles, et al., 2012; Skiles & Painter, 2018; Warren, 1982). These other controls are not discussed herein, but better understanding of them might derive from our results on mineral composition and physical properties.

Over the course of the snow-accumulation and ablation season between fall and late spring in the SJM, discrete, individual dust layers (IDLs) are deposited from regional dust storms (Figure 2a). Such IDLs typically accumulate over a short period of time (typically hours to less than 1 day but as much as several days). The IDLs emerge together as a concentrated layer of dust consisting of coalesced discrete layers on the surface usually in late spring or early summer (Figure 2b). This All-Layers-Merged (ALM) layer, composed of dust deposited over the course of a season, is then exposed to sunlight, commonly for many weeks until snow cover is entirely melted. These phenomena have been systematically investigated at a study site (Swamp Angel Study Plot, SASP; Figure 1) that yielded the samples used in this investigation (Axson et al., 2016; Landry et al., 2014; Painter, Skiles, et al., 2012; Skiles et al., 2012, 2017; Skiles & Painter, 2016, 2018).

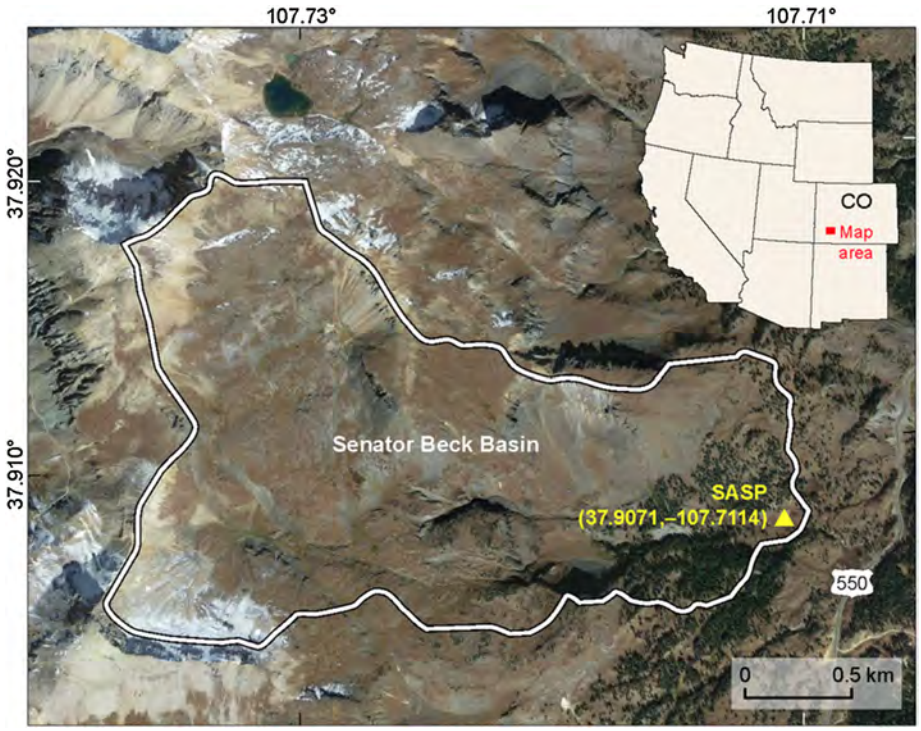

Figure 1. Map showing part of the San Juan Mountains (Colorado) with the outline of the Senator Beck Basin (white line), the locations of the Swamp Angel Study Plot (SASP; yellow triangle), and Highway 550.

1.1. Importance of the Study Site to Downstream Water Resources

The SASP (37.9071°N, 107.7114°W; 3,368-m elevation) is instrumented to measure variables responsible for the timing and rate of snow melt (Landry et al., 2014; Painter, Skiles, et al., 2012; the Colorado Dust-on-Snow (DOS) Program operated by the Center for Snow and Avalanche Studies in Silverton, Colorado (http://www.codos.org/). This plot is located in a clearing within an otherwise wind-protected, coniferous forest in the headwaters of the Uncompahgre River, an important tributary to the Colorado River.

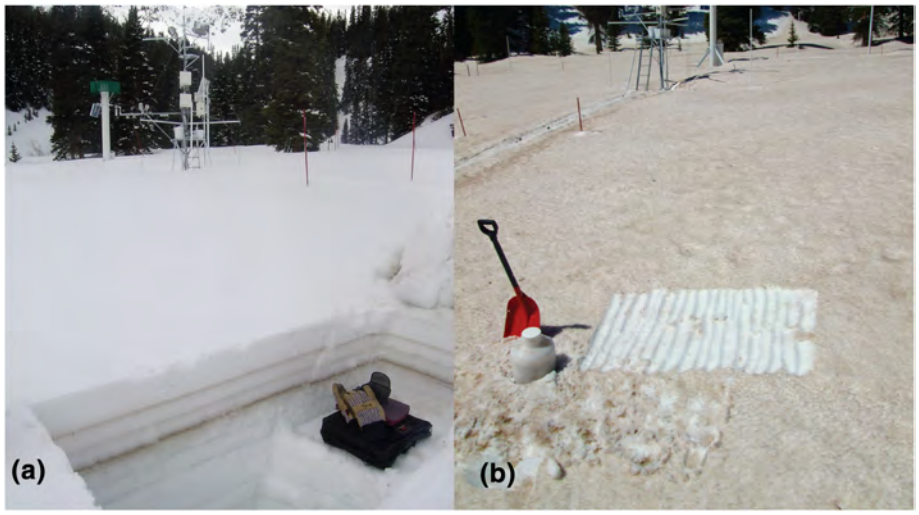

Figure 2. (a) Snow pit revealing individual dust layers beneath a clean snow surface at SASP, 22 April 2013. (b) Surface of the All-Layers-Merged dust layer showing sampling area at SASP, 28 May 2014. Photographs provided by Center for Snow and Avalanche Studies.

As general background, Painter, Skiles, et al. (2012, 2018) and Skiles and Painter (2017, 2018) summarized energy balance in snow cover, and the ways by which light-absorbing particles (LAPs) (including black carbon and tree litter, in addition to mineral dust) can affect the timing and rates of snow melt and runoff that is critical for downstream water management. Relative to pre-European settlement (about 1860 CE), a combination of measurements and modeling point to direct effects of dust loading on the reduction of snow cover and the onset of snow melt by 25–51 days (Painter et al., 2007, 2010; Skiles et al., 2012). All such melting puts water into downstream storage earlier than is desirable because early, heavy pulses of runoff must sometimes be quickly passed through storage reservoirs. Under these conditions, total available water supply is lessened during the hottest and driest parts of summer when water is most needed.

2. Materials and Methods

2.1. Field Sampling

Sampling involved delineating a 0.5-m^2 area with rulers, cutting away snow adjacent to the marked boundaries to isolate the sample area, and then collecting the concentrated dust layer with small shovels into heavyweight trash bags. The samples used in this study spanned water year (WY) 2011 through WY2016. For example, WY2011 is defined as the time period from 1 October 2010 to 30 September 2011. The six ALM samples were collected just prior complete disappearance of snow cover, the timing for which varied from year to year, as early as the beginning of May (WY12) to as late as mid-June (WY11). The 25 individual DOS layers were sampled in a similar fashion immediately following a DOS event. The dust/snow samples were transferred to14-L carboy jugs, which were then transported to U.S. Geological Survey laboratories (Denver, Colorado).

2.2. Sample Preparation and Determination of Sample Mass

Melted snow with dust was evaporated at 45°C for weighing to determine a mass loading value. Before weighing, large particles of plant matter, such as conifer needles, were removed by hand. Each dried dust sample was divided so that all measurements were made on splits from the same sample.

2.3. Reflectance Spectroscopy

Reflectance spectra were measured on dried samples in aluminum cups to determine mineral composition and average reflectance values. An aliquot of each sample sufficiently thick to fill a sample holder was used so that measured reflectance represented the dust, regardless of total sample mass. Reflectance spectra were measured in the laboratory by two methods. The IDL samples (about 1–2 g) were measured using an Analytical Spectral Devices Inc. FieldSpec3 spectrometer, covering the wavelength range of 0.35–2.50 μm in 2,151 channels. The ALM samples (about 3–4 g) were measured using a HySpex imaging spectrometer system with two detectors covering the visible/near-infrared (0.4–1.0 μm; 186 channels) and shortwave infrared (SWIR; 1.0–2.5 μm; 288 channels). The ALM samples had been previously measured using the Analytical Spectral Device. We identified minerals by analyzing reflectance spectra using the Material Identification and Characterization Algorithm, a module of the PRISM software system (Kokaly, 2011), which uses continuum removal to isolate diagnostic absorption features and linear regression to compare spectral features. In this way, the spectra of the samples were compared with reference spectra of minerals and other materials (Clark et al., 2007). The Material Identification and Characterization Algorithm analysis computes a fit value, ranging from 0 to 1, between the sample spectrum and each reference material (Kokaly, 2011), with "best fit" determined by the highest fit value.

2.4. Principal Components Analysis

We performed principal components analysis on magnetic, chemical, spectral, and particle size properties using the package "vegan" in R (Oksanen et al., 2019). Sites were unscaled, and weighted dispersion was equal in all dimensions. Ordinations were displayed by the principal components that explained the highest proportion of variance.

2.5. Magnetic Properties

Magnetic properties were measured to distinguish among the iron oxide minerals and to determine their abundances (magnetite and maghemite, antiferromagnetic ferric oxide minerals, such as hematite and goethite, and superparamagnetic nanophase (<30 nm) particles; e.g., Evans & Heller, 2003; Maher, 2011).

Powdered samples for magnetic analysis were prepared by packing approximately 100 mg of bulk sediment into #4 gelatin capsules and then placing them in plastic straw holders. All sample measurements were normalized by mass. Room-temperature hysteresis measurements were obtained in a vibrating sample magnetometer (Princeton Corporation Measurements 3900). Hysteresis parameters (saturation magnetization, M_s; saturation remanence, M_r; coercivity, B_c; and high-field susceptibility, χ_{hf}) were determined from hysteresis loops after high-field slope correction over the interval of 0.8–1.2 Tesla (T) using the nonlinear approach-to-saturation fitting method of Jackson and Solheid (2010). Weight percent magnetite was determined as sample $M_s/92$ Am^2 kg^{-1} (the M_s of pure magnetite) × 100%. Coercivity of remanence (B_{cr}), hard isothermal remanent magnetization (HIRM), and the S_{300} ratio were determined from DC-backfield remanence curves obtained by demagnetizing the IRM acquired in 1.2 T in a stepwise manner in increasing back fields to −1.2 T. The HIRM values and the S_{300} ratio were calculated using the following definitions: $\text{HIRM} = 0.5 \times (IRM_{max} + IRM_{-0.3T})$ and $S_{300} = (IRM_{-0.3T})/IRM_{max}$. Low-temperature (LT, 20–300 K) remanent magnetization induced in fields of 2.5 T and AC susceptibility was measured with a superconducting quantum interference device magnetometer (Quantum Design, San Diego, CA, USA – MPMS-XL). Details of the analytical procedures are provided in Texts S1 and S2 in the supporting information.

2.6. Mössbauer Spectroscopy

Mössbauer spectra were measured to characterize iron oxide mineralogy and to detect the presence of nanophase ferric oxides (details of characterization in Text S3). Measurements were made with bulk-sediment samples at 300 K and $T < 20$ K in zero applied field using a constant-acceleration spectrometer (model MS6, SeeCo, USA) in transmission geometry with a ^{57}Co/Rh source. Temperature was controlled by a closed cycle He gas refrigerator cryostat (Janis Research Co, USA). Spectra were obtained using a triangular waveform and a 1024 channel analyzer. An alpha-Fe foil at room temperature was used to calibrate isomer shifts and velocity scale. Mössbauer spectra were fit by least squares to sums of Lorentzian lines using custom software to obtain estimates for isomer shift (IS), quadrapole splitting (QS), hyperfine field (B_{HF}), linewidth (Γ), and relative area (A) for each subspectrum. In some cases, magnetically split sextet subspectra were fit using a distribution of hyperfine fields (HFD).

2.7. Chemistry

Carbon content was measured with an Elementar Soli TOC Cube (Elementar Analysensysteme GmbH, Langenselbold, Germany), under a gas-switching method, with temperature-dependent oxidation. Dried samples were weighed into ceramic crucibles and loaded into the instrument autosampler. During the measurement of each sample, the temperature of the combustion oven was first ramped to 400°C in an oxygen environment and the resulting CO_2 was measured on the Soli TOC Cube near-infrared detector. The carbon oxidized and measured during in this step is considered organic carbon (OC_{400}). Next, the carrier gas was switched from oxygen to nitrogen and the oven temperature ramped to 900°C. The resulting CO_2 corresponds to total inorganic carbon (TIC). Finally, the carrier gas was switched back to oxygen with the oven remaining at 900°C, and any remaining carbon—the residual oxidizable carbon (ROC)—was converted to CO_2 and measured. With this method, the total carbon (TC) content of the sample is the sum of the three carbon components measured ($TC = OC_{400} + TIC + ROC$). The total organic carbon (TOC) content of the sample, equivalent to TOC measured using the traditional method where a sample is first treated with acid to remove the inorganic carbon component and then combusted at a fixed temperature, is the sum of OC_{400} and ROC ($TOC = OC_{400} + ROC$).

Major- and trace-element concentrations of aliquots were determined following 4-acid digestion (a mixture of hydrochloric, nitric, perchloric, and hydrofluoric acids) by analyzing the resulting solution by inductively coupled plasma atomic emissions spectrometry (Briggs, 2002) and inductively coupled plasma mass spectrometry (Briggs & Meier, 2002; Wolf & Adams, 2015).

2.8. Scanning Electron and Reflected-Light Microscopy

Complemented by reflected-light microscopy, scanning electron microscopy (SEM; FEI Quanta) revealed occurrences of iron oxide minerals and carbonaceous matter. The SEM analyses performed in conjunction with an attached energy dispersion X-ray system (EDS) and secondary and backscatter electron detectors at resolutions above 9 nm. Samples were dispersed in isopropyl alcohol, transferred to polished carbon planchets, and carbon coated prior to examination. For a few SEM-EDS samples, carbonaceous matter was

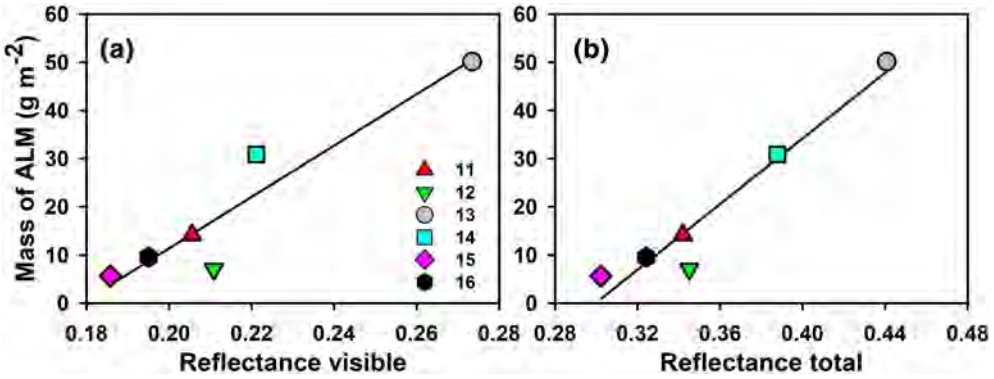

Figure 3. Bivariate plots of (a) visible reflectance vs. mass loading, $r^2 = 0.89$; (b) total reflectance vs. mass loading, $r^2 = 0.9$. Legend shows water year markers as in the following figures.

concentrated by floating in a ZnBr solution with a specific gravity of 2.0. Magnetic minerals in three DOS bulk samples were concentrated by suspended magnet passed which flowed a circulating mixture of sediment and distilled water (Reynolds et al., 2001). The magnetic separate was examined in polished grain mounts under reflected-light microscopy for identification of opaque minerals larger than about 2 μm.

2.9. Particle-Size Analysis

Dust-particle sizes were measured using laser-diffraction methods (Malvern Mastersizer model 2000) capable of measuring particles between 0.06 and 2,000 μm and are reported as volume percentages. Prior to analysis, samples were prepared by digesting organic matter in 30% H_2O_2 and were deflocculated in a Na-hexametaphosphate solution.

3. Results and Interpretations

3.1. Mass Loading Determinations, Water Years 2011–2016

Mass loading of the ALM layers ranged greatly from 5.6 to 50.1 g m^{-2} for WY15 and WY13, respectively (Figure 3; Table 1). During WY13, an extraordinarily large dust event (WY13, D6, 8 April) deposited nearly 50 g m^{-2} of dust. This single event deposited much more dust than the mass of the previous two WYs combined (WY11–12) and slightly more than the combined masses as all of the following ALM layers (WY14–16). Soon after, another large dust event (WY13, D8, 15–17 April) deposited about 9 g m^{-2} of dust, the second largest DOS event of the WY11-WY16 record (http://www.codos.org/#codos; accessed 1 April 2019). Reasons for the differences between the ALM and the combined IDL mass loadings are discussed in Text S4.

3.2. Reflectance Spectroscopy

The average reflectance values for the six ALM samples were 0.215 (standard deviation [sd], 0.031) over the visible part of the spectrum (Rvis) and 0.357 (sd, 0.050) over the total spectrum (Rtot) (Table 1; examples in Figure S1). The ranges in Rvis (0.186 to 0.273) and Rtot values (0.302–0.441) varied by factor differences of nearly 1.5. Factor difference is the ratio of the maximum to minimum value. There was no apparent temporal trend represented in these values. For the 25 measured IDLs, Rvis averaged 0.178 (sd, 0.024) and Rtot averaged 0.384 (sd, 0.034) (Table S1) and were statistically identical to the ALM Rvis and Rtot mean values (0.175, sd, 0.016; avg., 0.359, sd, 0.045, respectively) using the earlier, identical methods.

Reflectance values corresponded with ALM mass loadings, relatively high reflectance with high mass and lower reflectance with lower mass (Figure 3). Possible reasons for this finding are considered in section 4.

Goethite was the dominant Fe oxide mineral identified by reflectance spectroscopy in five of the six ALM DOS layers, with hematite dominant in the other (WY14). The prevalence of goethite is also found in its dominance over hematite in 18 of 25 individual DOS layers. The average reflectance values for goethite-dominated and hematite-dominated IDL samples were closely similar: For the former Rvis = 0.1758, Rtot = 0.3792; for the latter Rvis = 0.1776, Rtot = 0.3891.

Table 1
List of the ALM Samples by Water Year (WY), Dates of Collection, Dust (D) Layers by Event in ALM Sample, Masses, Dominant Ferric Oxide Mineral Identified in Reflectance Spectra by Best Fits to Standards, and Total and Organic Carbon

Collect date	Dust events	Mass (g m^{-2})	Total reflectance	Visible reflectance	Fe oxide	Total C %	Organic C %
6/14/2011	D1–D11	14.13	0.3420	0.2055	Goethite	4.68	4.02
5/5/2012	D4–D8	7.07	0.3450	0.2108	Goethite	5.83	5.24
5/13/2013	D4–D9	50.11	0.4408	0.2734	Goethite	2.63	1.92
5/28/2014	D3–D8	30.86	0.3878	0.2212	Hematite	2.94	2.4
6/4/2015	D1–D3	5.62	0.3022	0.1858	Goethite	10.71	10.35
5/31/2016	D1–D6	9.57	0.3242	0.1950	Goethite	6.65	6.42
	Average	19.56	0.3570	0.2153		5.57	5.06
	Standard deviation	17.55	0.0498	0.0310		2.97	3.09
	Factor difference	8.92	1.46	1.47		4.07	5.38

Note. Organic C % is the weight percent sum of the OC_{400} and ROC components.

3.3. Principal Component Analysis

Negative correspondences existed among reflectance values and those for ferric oxide (HIRM) and silt, whereas reflectance values were opposite along the first principal component explaining 86.1% of the variation among ALM DOS layers for magnetite (Ms) and organic carbon (Figure 4a). The PCA plot for elemental components (Figure 4b) showed (1) affinities of some metals (Pb, Cr, Zn, Cu, and Ni) for organic carbon, and thereby negatively with reflectance, (2) the close association between Fe and Al, along with their likely associations with clay amounts, lacking correspondence with reflectance, and (3) major and minor "soil" components Na, Mg, K, Ti, Mn, Ca, and Ba that clustered together and collectively showed positive affinity with reflectance.

3.4. Types and Amounts of Iron Oxide Minerals From Magnetic Measurements

Goethite, hematite, and magnetite were identified in all ALM DOS layers by their magnetic properties. Ferric oxide abundances as indicated by HIRM values (Table S2) showed negative correlation with reflectance values (Figures 5a and 5b). The factor differences in HIRM and reflectance values were identical at 1.5×, implying direct control of ferric oxide on RF, even though the HIRM values do not account for nano-size occurrences.

The presence of magnetite in all ALM samples was confirmed from LT measurement of magnetization and susceptibility, which showed the characteristic magnetic signature for the Verwey transition in magnetite at $T = 110–120$ K (Figures S2 and S3). In addition, the hump-shaped remanence cooling curves (Figure S3) also indicated that some of the magnetite was partially oxidized (Özdemir & Dunlop, 2010). The LTSIRM cycling curves (15–400 K) for all ALM samples also indicated the presence of both hematite and goethite, after AC demagnetization removed the magnetite contribution (details in Text S2; Figure S2).

Hysteresis loops displayed magnetic behavior typical of ferrimagnetic minerals like magnetite. There was little variation in coercivity (B_c and B_{rc}) and hysteresis parameters (M_r/M_s and B_r/B_c) among the ALM samples (Table S3). As these parameters are sensitive to particle-size variations in the magnetite fraction, the hysteresis data reflect similar magnetite particle-size distributions (PSDs) with particles sizes in the range of 0.1–10 μm in all samples (e.g., Dunlop, 2002). From saturation magnetization, magnetite occurred in amounts from 0.052 wt.% (WY13) to 0.132 wt.% (WY15).

Reflectance values exhibited associations with magnetite abundance from saturation magnetization; the correspondence between magnetite wt.% and Rtot was tighter than that between magnetite wt.% and Rvis (Figures 5c and 5d). This relation is consistent with the effect of a dark body suppressing reflectance across the entire measured spectrum. Values of saturation remanent magnetization were likewise negatively associated with reflectance because they are also controlled mainly by magnetite abundance (RTSIRM, Table S2; M_r, Table S3).

3.5. Types and Amounts of Iron Oxide Minerals From Mössbauer Spectroscopy

Results from Mössbauer spectroscopy provided further information on the amounts of hematite and goethite. Similar room-temperature spectra for all samples indicated the presence of hematite, assigned by

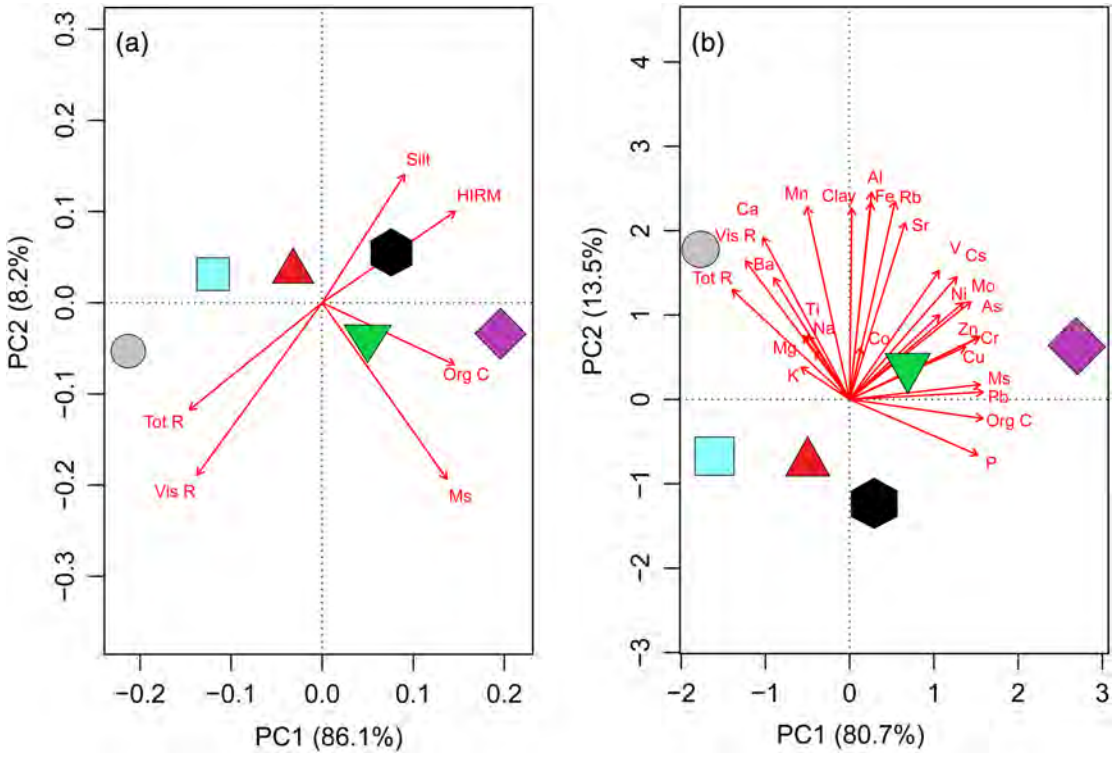

Figure 4. Results from principal components analysis of (a) reflectance, magnetic properties, and organic carbon (org C) content (red arrows) in relation to each ALM layer; (b) reflectance, chemical properties, and clay (red arrows). Properties with arrows in the same direction indicate general correlation and layers closer together indicate greater similarity in properties. The proportion of variance explained is indicated on the first (PC1) and second (PC2) principal-components axes. Large markers for water years as in Figure 3. Abbreviations: HIRM = Hard Isothermal Remanent Magnetization, Ms = saturation magnetization, Org C = organic carbon, Tot R = total reflectance, Vis R = visible reflectance.

a magnetically split sextet, along with other Fe^{3+}- and Fe^{2+}-bearing minerals, assigned by two doublets (Text S3; Figure S4; Tables S4 and S5). Hematite contributed 16% (WY13) to 30% (WY14) of the total spectral area, whereas the Fe^{3+} doublet accounted for 54% (WY14) to 70% (WY13). The remaining spectral area, about 15%, occurred as Fe^{2+} in iron-bearing minerals. There was significant overlap in the hyperfine parameters (IS and QS) for many Fe^{3+}- and Fe^{2+}-bearing minerals (e.g., phyllosilicates, nanophase iron oxides) such that it was not possible to assign specific candidate minerals to the two doublets in multiphase natural samples based on room-temperature Mössbauer data alone.

Spectra collected at temperatures below 20 K were best fit by a superposition of two sextet and two doublet components for five of the six ALM DOS layers (Text S3; Figure S5; Tables S4 and S5). An exception was the WY14 sample where a third small ferric doublet (7.2% relative area) slightly improved the final fit. The sextet with the highest hyperfine field (B_{Hf} ~ 53 T) was assigned to hematite, whereas the second sextet had hyperfine parameters consistent with goethite (B_{Hf} ~ 50 T). No other magnetic oxides (e.g., ferrihydrite) were detected. The appearance of goethite in spectra collected at $T < 20$ K but not at 300 K is ascribed to a significant fraction of nano-size goethite with particle sizes below 50 nm (Berquó et al., 2007; Guyodo et al., 2006; van der Zee et al., 2003). The hematite spectra indicated that the hematite was fined grained (<1,000 nm) but without a significant nano-sized particle fraction. Further details are given in Text S3. These results are similar those reported for DOS samples from the Wasatch Range (Utah, USA) by Reynolds, Goldstein et al. (2014).

Spectral areas at low temperatures have slightly higher values attributed to hematite than goethite (goethite/hematite ~0.8), except for WY13 with relatively more goethite (goethite/hematite = 2.4) (Figures 6a and 6b). However, the relative amount of iron occurring as ferric oxides (goethite + hematite) varied little among the samples, varying from 41–51% of the total amount of iron-bearing minerals (Figure 6b). Combining chemical analysis for total Fe (inductively coupled plasma mass spectrometry) and sextet subspectral areas, hematite and goethite occurred in similar modal amounts of ~0.8 wt.% in each of the ALM samples except WY13,

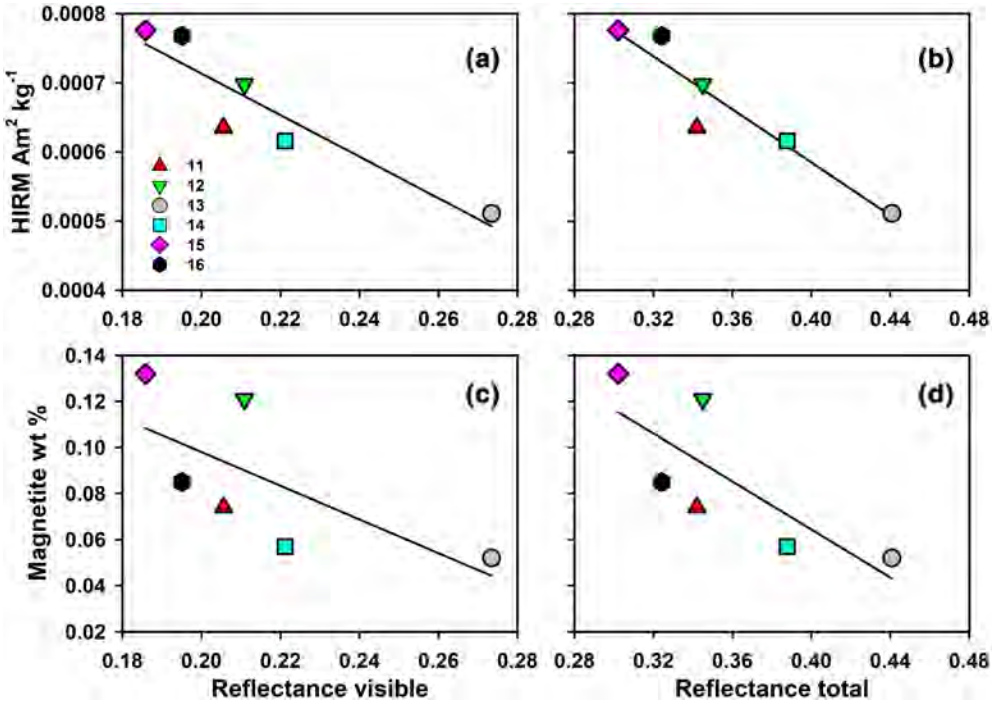

Figure 5. Bivariate plots of (a) HIRM vs. visible reflectance ($r^2 = 0.85$, $p = 0.009$) and (b) vs. total reflectance ($r^2 = 0.90$, $p = 0.004$) and of (c) magnetite wt.% vs. visible reflectance, ($r^2 = 0.47$, $p = 0.133$) and (d) vs. total reflectance ($r^2 = 0.61$, $p = 0.066$).

which had a significantly higher amounts of goethite (1.26%) and a lower amount of hematite (0.47%). Magnetic oxide characteristics are summarized in Table 2; concentrations of the Fe oxide minerals for each ALM sample are listed in Table S6.

3.6. Organic Carbon and Elemental Chemistry

Organic carbon in the ALM samples, defined as OC_{400} + ROC, ranged from 1.92 wt.% in WY13 to 10.35 wt.% in WY15 (factor difference, 5.4; average = 5.06 wt.%; sd = 3.1; Tables 1 and S7). Three ALM samples (WYs 11, 12, and 16) were clustered between 4.0 and 6.4 wt.%. Amounts of ROC were very low (0.16–0.50 wt.%). These measures of organic carbon cannot discern the proportion of black carbon that resided in organic carbon as assessed in section 4.

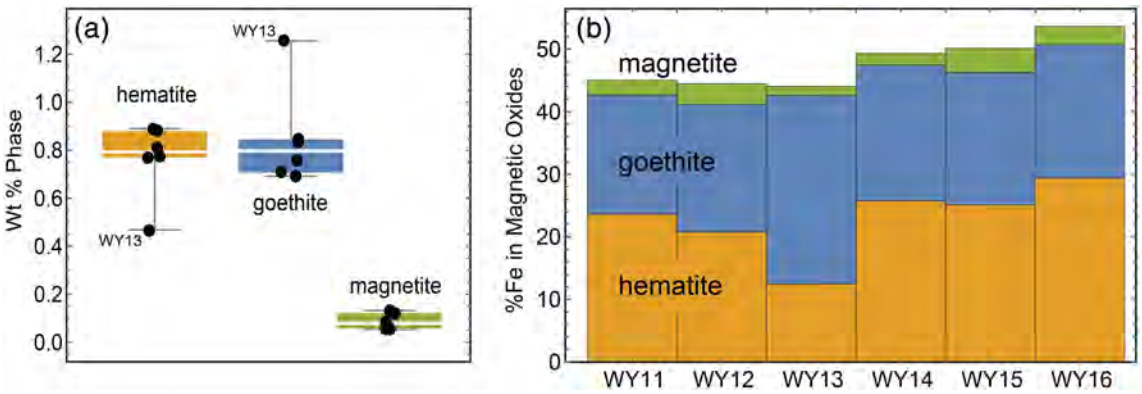

Figure 6. Magnetic oxide concentrations in the DOS-ALM samples. (a) Box plot of modal abundances of hematite, goethite, and magnetite. The 25th (lower edge of the box), 50th (horizontal line through the box), and the 75th (upper edge of the box) percentiles of the distributions of values are shown. Whiskers below and above the box represent the minimum and maximum value. (b) Histogram of iron speciation of hematite, goethite, and magnetite in DOS-ALM by water year. The remaining iron occurred as paramagnetic iron-bearing silicates (Figure S6). Hematite and goethite concentrations from Mössbauer analysis below 20 K and magnetite concentration from saturation magnetization at 300 K.

Table 2
Summary of Magnetic Oxides in ALM DOS Samples

Fe oxide	Particle size range	Nanoparticles	% Total Fe	% Total sample
Magnetite	Microcrystalline (<~10 μm)	Minor	2.6	0.052–0.132
Hematite	Microcrystalline (<1,000 nm)	Minor	22.9	0.72–0.93
Goethite	Nanogoethite (<50 nm)	Abundant	22.8	0.69–1.23

Note. Nanoparticles are identified by superparamagnetic behavior and typically occur in particle sizes less than 30 nm for magnetite, hematite, and goethite. Magnetite is probably partly oxidized. % Total Fe is the average for the six ALM samples from ICP analyses (Table 3). % Total sample, weight % concentration ranges of hematite and goethite from Mössbauer and ICP spectroscopy in the ALM samples; weight % magnetite from saturation magnetization. Table S6 lists the concentrations of iron oxide minerals in each ALM sample.

TOC was negatively associated with reflectance, at $r^2 = 0.60$ for Rvis and more tightly so at $r^2 = 0.75$ for Rtot (Figures 7a and 7b). This relation was controlled by end-member outliers—The WY13 sample had high reflectance and low organic carbon amounts, and the WY15 sample had low reflectance values and high organic carbon amounts (Figure 7a). By these relations, organic carbon also appeared to be associated with ALM sample mass (Figure 7c). Several possible explanations arise, including the effects of (1) continuous or episodic deposition of carbonaceous matter onto snow cover during relatively low-dust-mass years such that organic carbon was concentrated in the resulting ALM layer (e.g., WY15; 10.35 wt.%) and (2) an approximately equivalent amount (assumed) of organic matter deposited onto snow cover during a relatively high-dust-mass year such that organic carbon was diluted in that year's ALM layer (WY13; 1.92 wt.%). Late-season accumulation of organic matter (Winkler et al., 2010), especially pollen, may have been similarly concentrated or diluted. We do not interpret the associations as happenstance that dust sources active during low-dust years were enriched in organic carbon and that sources active during high-dust years were

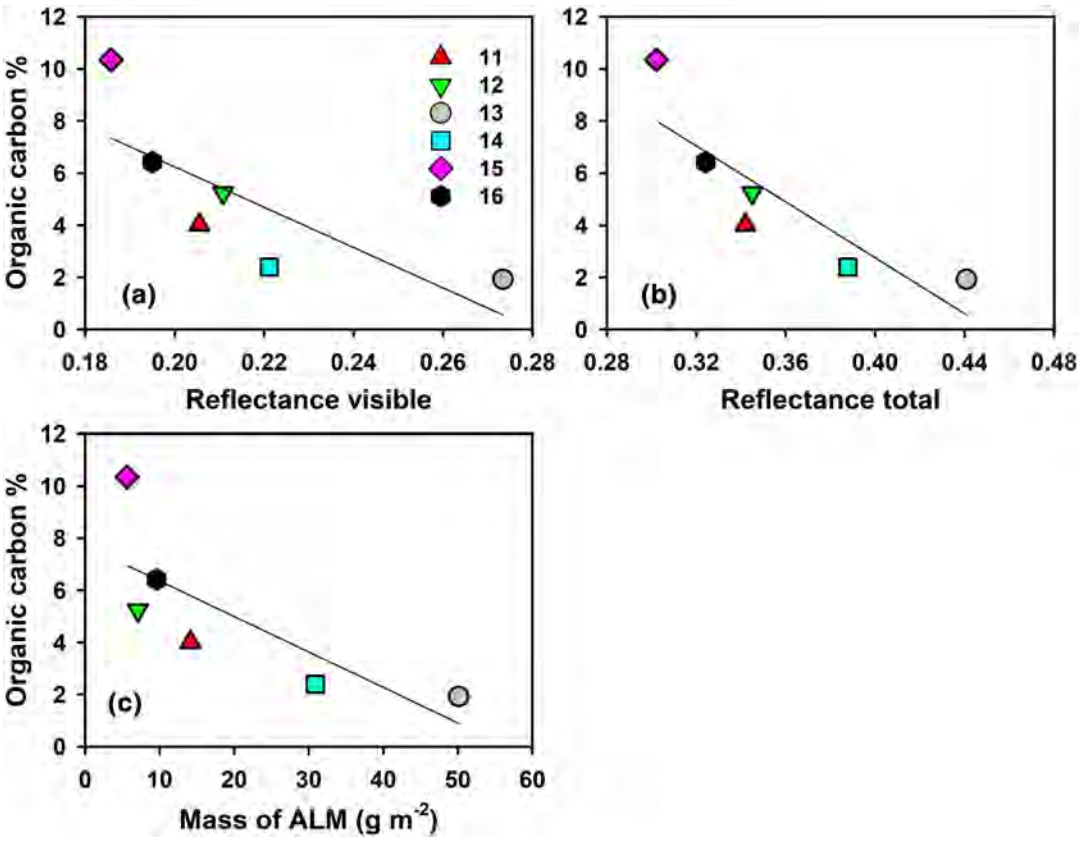

Figure 7. Bivariate plots of (a) organic carbon vs. visible reflectance ($r^2 = 0.60$, p value = 0.069), (b) vs. total reflectance ($r^2 = 0.75$, p value = 0.026), and (c) vs. ALM mass ($r^2 = 0.60$, p value = 0.071).

Table 3
Major Elements Determined by ICP-AES

Water year	Al %	Ca %	Fe %	K %	Mg %	Na %	P %	Ti %
11	5.28	0.873	2.28	1.88	0.858	0.864	0.0669	0.304
12	6.1	0.944	2.61	2.08	0.778	1.08	0.0712	0.364
13	6.28	1.56	2.62	2.06	0.964	0.962	0.055	0.345
14	5.43	1.13	2.2	2.29	1.06	1.04	0.0585	0.306
15	6.01	0.851	2.48	2.01	0.955	0.898	0.086	0.284
16	5.18	0.66	2.09	1.95	0.77	0.91	0.0787	0.33
Average	5.71	1.00	2.38	2.05	0.90	0.96	0.07	0.32
Standard deviation	0.47	0.31	0.22	0.14	0.12	0.09	0.01	0.03
Factor difference	1.21	2.36	1.25	1.22	1.38	1.25	1.56	1.28

lacking organic carbon. The previously mentioned result that reflectance values from ALM and IDL samples, considered as two groups, were statistically identical (as obtained from the original method) strongly suggests that any addition of late-season, locally derived organic carbon did not greatly shift ALM reflectance values over the 6-year study period. Total reflectance in the WY15 ALM sample, however, appeared to have been diminished by the presence of abundant pollen as discussed later.

The compositional similarities of the ALM samples are illustrated by the small variation in concentrations of many major and minor elements (Al, Fe, K, Mg, Na, P, Ti, Mn, and Ba; factor differences <1.6; Tables 3 and 4 [listing ICP data discussed in main text] and Table S7 [listing all ALM ICP data]). Iron was strongly correlated with only Al, Sr, Rb, and Co (Figures 4b and 8). Importantly, Fe amounts did not correspond with reflectance values nor with the abundances of ferric oxide minerals (HIRM, Mössbauer) and magnetite. Most Fe apparently occurred in paramagnetic phases as indicated by the large ferric doublets in Mössbauer spectra that did not magnetically order below 20 K. Some of these phases likely occurred as Fe-bearing clays, as indicated by the association of high-field magnetic susceptibility (paramagnetic susceptibility) with Fe and clay amounts, as well as Fe with Al.

Trace metals may provide clues to the origins and forms of organic carbon. As with major elements, concentrations of most trace metals varied by factors <1.6; only Cu, Cd, Mo, Bi, Sb, and Ag varied by more than 3.7× (Tables 4 and S6). Strong correlations were found among organic carbon and many trace metals and especially those typically residing in anthropogenic aerosols that are commonly associated with industrial effluents (e.g., As, Cu, Mo, Pb, Ni, Cs, and Zn; Figures 4b, 9a, and 9b). Trace metals were correlated among themselves (examples in Figures 9c and 9d) but not among major elements (e.g., Al, Fe, K, Na, Mg, and Ti), which are considered to represent dominantly rock-derived surficial sediments and soil (Figure 4b).

3.7. Microscopy Observations of Iron Oxides and Organic Matter

Ferric oxide minerals were identified on the basis of (1) petrographic observations and Fe concentrations of metalliferous particles, under SEM-EDS, that were too high to represent structural Fe within certain

Table 4
Selected Trace Elements Determined by ICPMS

Water year	As (ppm)	Ba (ppm)	Cd (ppm)	Cs (ppm)	Cu (ppm)	Mn (ppm)	Mo (ppm)	Ni (ppm)	Pb (ppm)	Rb (ppm)	Sr (ppm)	Zn (ppm)
11	6.1	602	0.13	4.7	48.5	310	1.7	15.8	32.6	78.8	142	82.8
12	7.8	651	0.49	5.4	72.1	361	3.1	15.1	37.3	83.8	171	97.1
13	6.7	659	0.31	5.3	45.2	493	1.6	15.7	22.1	87	163	73.5
14	5.9	607	0.38	3.9	32.4	381	1.3	13.5	24.8	78.4	146	60.5
15	9.3	573	0.49	6.4	122	389	4.4	16.9	47.5	86.2	166	122
16	6.5	596	0.27	4.9	53.3	318	0.8	15.2	29.3	79.8	141	77.3
Average	7.1	615	0.35	5.1	62.3	375	2.2	15.4	32.3	82.3	155	85.5
Standard deviation	1.3	33	0.14	0.8	32.0	66	1.3	1.1	9.2	3.8	13	21.5
Factor difference	1.58	1.2	3.77	1.64	3.77	1.59	5.24	1.25	2.15	1.11	1.21	2.02

Note. Table S8 contains all ICP data for ALM samples.

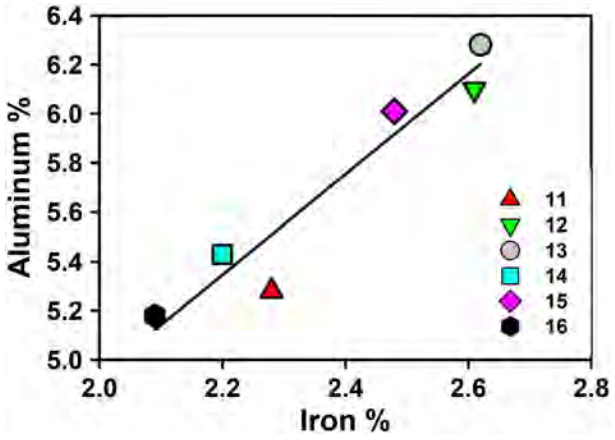

Figure 8. Bivariate plot of Al vs. Fe, $r^2 = 0.92$, p value = 0.002.

minerals such as clays and (2) optical properties under reflected light. Ferric oxide was found as individual particles and as aggregates of crystallites, a micrometer or less (as small as a few 10s nm), on surfaces of larger dust grains, such as quartz, or on and intercalated with clay minerals, many of which coated the larger grains (Figure 10).

Identified under reflected light in hues of red, orange, and yellow, very fine-grained ferric oxides were common within and on margins of altered rock particles, on margins of Fe-bearing particles, and interspersed within TiO_2 on margins of iron-titanium particles, such as titanomagnetite. Magnetite and Ti-rich magnetite were found as silt-size particles, and smaller magnetite particles (<5 μm sizes) were observed commonly within silt-size igneous rock fragments, such as those of basalt. Crystalline (specular) hematite was also observed within rock particles, as well as within particles of magnetite.

Fly-ash particles provided evidence for anthropogenic dust inputs. Fly ash is produced by the combustion of fossil fuels, typically in coal-fired power plants (Flanders, 1999; Goldhaber et al., 2004; Lauf, 1982; Locke & Bertine, 1986; Wang, 2014). Under SEM and reflected light, such fly ash in our samples included (1) spheres of aluminosilicate glass (as large as 45-μm diameter; Figure S7) and (2) magnetite-rich spheres having characteristic cuneiform textures indicating rapid quenching in air (samples WY11 D3; WY12 D3; and WY13 D1, D2, and D6).

Angular particles of coal, as small as 2 μm across, with obvious plant-matter texture were found in samples ALM WY11 and WY13 D2. One such particle had the shape and size typical for feed coal stored in the open at a power plant, but its origin as a particle from a natural dust source could not be dismissed (Figure S8). The closest coal-fired power plant to SASP is located about 140 km to the south-southwest. Particles of coal have been found in likely dust-source sediments about 250 km from SASP in the same direction. Particles of coal char were seen under SEM in the ALM WY11 and WY13 D1 samples. Particles of likely industrial origins

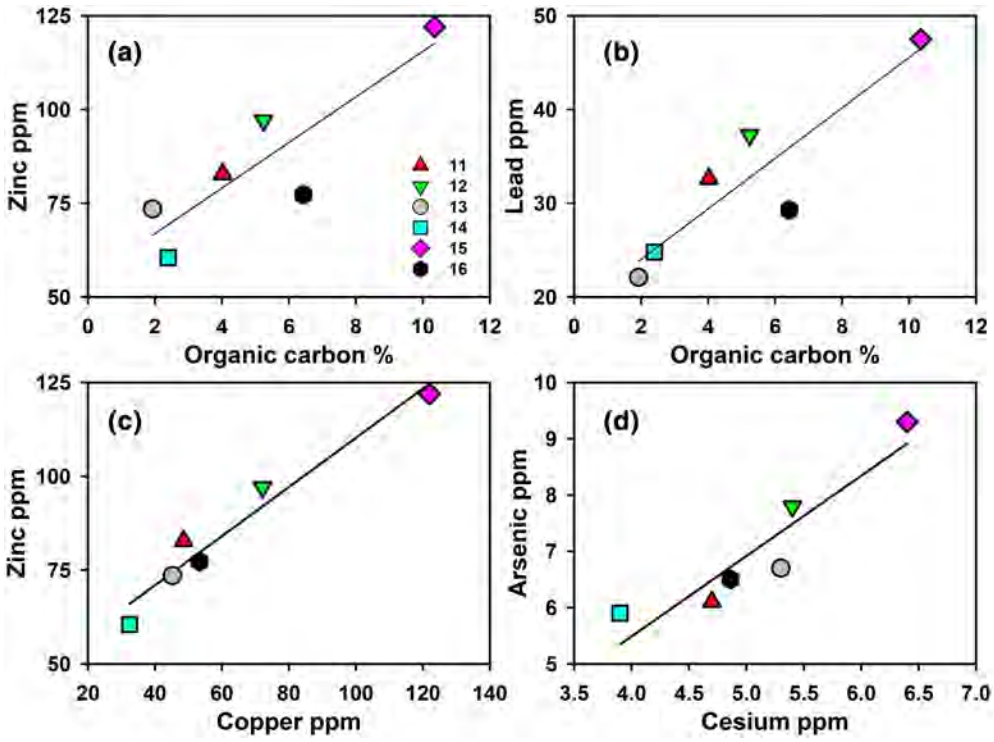

Figure 9. Bivariate plots of (a) organic carbon vs. Zn ($r^2 = 0.76$, p value = 0.023, (b) vs. Pb ($r^2 = 0.81$, p value = 0.014), (c) Cu vs. Zn ($r^2 = 0.95$, p value = 0.001), and (d) Cs vs. As ($r^2 = 0.86$, p value = 0.008).

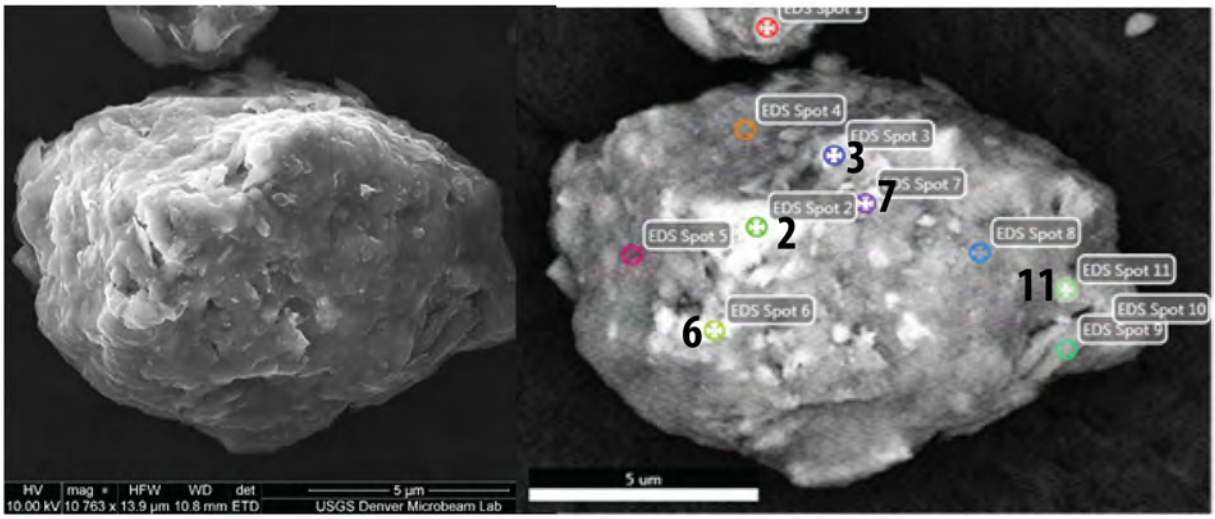

Figure 10. Left panel, secondary electron SEM micrograph of a quartz grain, about 12 μm in long-dimension. Right panel, low-kv, high-contrast-detector (VCD) image showing location of spots probed by energy dispersive spectroscopy (EDS). The grain is coated with clay, within and on which lie many submicrometer iron oxide particulates indicated by bright spots 2, 3, 6, 7, and 11 having high amounts of iron. Sample SASP WY13 D6.

were also recognized on the basis of carbon analyses, one of which contained a nano-size fleck of copper (sample ALM WY11; Figure S9). Individual particles of metals were also present in WY13 samples (D1 and D2), including one of iron-copper-sulfur, presumably sulfide, 5 μm in long dimension, and another of nickel, 200 nm in length.

3.8. Particle-Size Distributions

PSDs of ALM samples showed similar unimodal distributions with the exception of the sample WY13, which had a pronounced shoulder over the PM_{10} range including a high-clay percentage (Figure S10). The ALM median sizes ranged from 13.5 to 33.2 μm (WY13 and WY14, respectively) and averaged 21.4 μm (sd, 7.0) (Table 5). The range in median values (factor difference, 2.5) was driven by large disparities in PM sizes, in percentages, respectively for WY13 and WY14: $PM_{2.5}$ (14.4 and 6.5), PM_{10} (42.4 and 18.0), PM_{20} (60.4 and 32.0), PM_{63} (93.6 and 79.5), and sand (6.4 and 20.5). Median particle size was 18.6 μm (sd, 7.6) for the IDL samples (Table S9).

The large PSD variations in the ALM samples, with their influential outliers, corresponded only weakly, or not at all, with most parameters. As an exception, silt % was roughly associated with HIRM (ferric oxide; $r^2 = 0.54$; $p = 0.098$) and thus negatively with visible and total reflectance (Figure 5; Figures S11a–S11c).

Table 5
Particle Sizes, in Percentage, of the ALM Samples

Water year	Sand	Silt	Clay	$PM_{2.5}$	PM_{10}	PM_{20}	PM_{63}	Median
11	13.26	73.06	13.68	9.73	26.68	43.02	86.74	24.67
12	7.22	76.06	16.72	11.56	35.18	56.45	92.78	16.58
13	6.37	72.26	21.37	14.36	42.41	60.40	93.63	13.53
14	20.55	70.66	8.79	6.46	17.98	32.03	79.45	33.24
15	8.83	75.74	15.44	10.68	32.29	53.10	91.17	18.29
16	5.30	83.39	11.31	8.24	22.27	44.79	94.70	22.29
Average	10.25	75.19	14.55	10.17	29.47	48.30	89.75	21.43
Stand deviation	5.76	4.52	4.39	2.74	8.94	10.40	5.76	7.02
Factor difference	3.88	1.18	2.43	2.22	2.36	1.89	1.19	2.46

Note. Median values in micrometers.
Abbreviation: PM, particulate matter.

Relatively fine PSDs (seen in PM_{20}, PM_{10}, and $PM_{2.5}$) corresponded very roughly with Fe but not with certain metals (e.g., cadmium) and organic carbon (Figures S11d–S11f).

3.9. Comparisons of Properties in Individual-Dust-Layer Samples by Dominant Ferric Oxide

We examined physical and chemical properties for *t*-test significant differences between the goethite- and hematite-dominated IDL samples, as identified in reflectance spectra. The two groups had statistically identical values of reflectances and some elemental concentrations (e.g., Al, Ca, K, P, Ba, Nd, As, Cu, Sr, Ce, and La). With respect to significant differences, goethite-dominated samples were finer grained as evident in the content of silt, median particle size, PM_{63}, PM_{10}, $PM_{2.5}$, and clay and contained more Fe, Ti, Na, Cd, Cs, Mo, Ni, Pb, Sc, U, and Zn. Although these comparisons did not yield direct insight into RF variations, they might form a foundation for future RF and source-attribution studies.

3.10. Comparisons of Properties in ALM and Individual-Dust-Layer Samples

Concentrations of most elements in IDLs (Table S10) had wider ranges than those in ALM samples, but concentration averages were similar for most elements (Text S5; Figures 11a–11c). As an exception, Ca and Sr

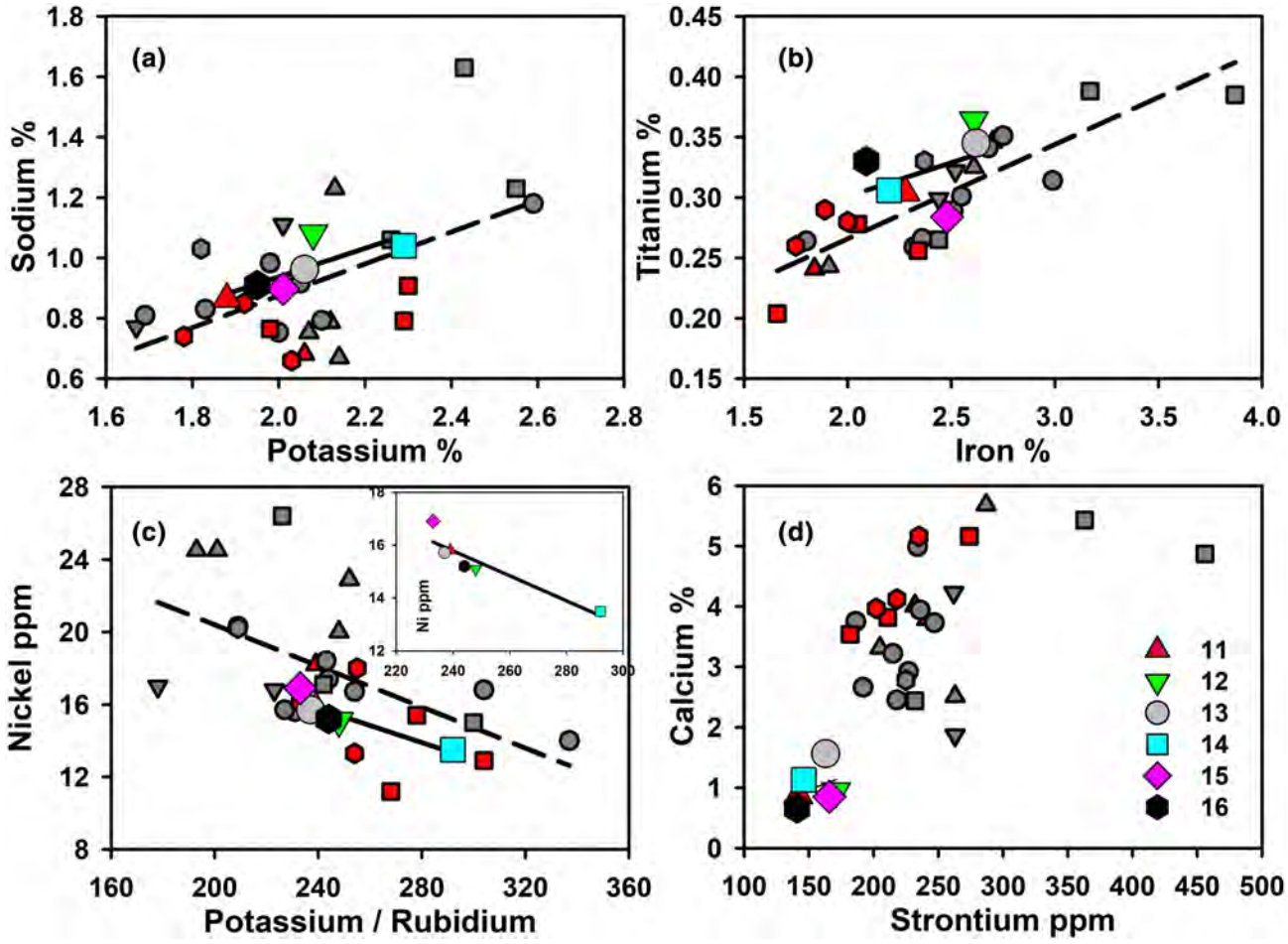

Figure 11. Bivariate plots for ALM samples (large markers; solid regression lines) and IDL samples (small markers; dashed regression lines). (a) Na vs. K, $r^2 = 0.60$ for ALM samples, $r^2 = 0.30$ for IDL samples; mean sodium values are not significantly different at $p = 0.776$, and median potassium values are not significantly different at $p = 0.338$; (b) Fe vs. Ti, $r^2 = 0.17$ for ALM samples, $r^2 = 0.69$ for IDL samples; averages of Fe and Ti for the IDL samples yield a Fe:Ti ratio (8.1) similar to that of the upper continental crust (10.3) from Rudnick and Gao (2003); (c) nickel vs. the potassium-rubidium ratio; $r^2 = 0.85$ for ALM samples (also shown in inset); $r^2 = 0.30$ for IDL samples. The relations shown may indicate the presence of mica, or, for example, biotite degraded to illite. Micas tend to accumulate Rb and hence have low K:Rb and relatively high Ni concentrations. (d) Bivariate plot of Ca vs. Sr. Lower contents of both elements in ALM samples relative to IDL samples are attributed to dissolution during extended exposure of ALM samples to snow melt. For IDL markers: gray, goethite as primary Fe oxide mineral; red, hematite, both on the basis of best fits to reflectance spectra; WY11, upright triangles; WY12, inverted triangles; WY13, circles; WY14, squares; WY16, hexagons; no WY15 IDL samples.

concentrations were higher in the IDL than in the ALM samples (Figure 11d). This difference indicates the loss of Ca and Sr by depletion of carbonate minerals in ALM samples probably in the presence of acidic snow melt, as previously documented by Clow and Ingersoll (1994) and Clow et al. (2016). Considering that the IDLs were collected within a few hours or days from the time of deposition, the Ca concentrations in the IDL samples likely represented original dust fall.

4. Discussion

The primary goal of this work was to identify the types, amounts, sizes, and occurrences of particulate matter in samples from DOS layers that strongly influence laboratory measurements of reflectance. Constituents that appeared directly to increase the absorption of solar radiation in DOS layers included ferric oxide minerals, dark rock particles (DRPs; e.g., basalt), and carbonaceous matter to the extent that some of it occurred as black carbon.

Ferric oxide minerals strongly diminished reflectance in the ALM samples. The principle evidence for this conclusion is that reflectance values correlated negatively with HIRM (Figure 6), which appeared to be carried primarily by microcrystalline hematite. Similar correlations of HIRM with reflectance values have been found in our three prior studies of dust using identical methods (Reynolds, Goldstein et al., 2014,Reynolds, Cattle et al., 2014; Moskowitz et al., 2016). Microcrystalline and (or) crystalline goethite may also have contributed to HIRM, but most goethite occurred in nano-sizes and thereby was not measured by HIRM. Hematite appeared to be slightly more abundant than goethite on the basis of magnetic and Mössbauer results. In contrast, goethite was identified as the dominant ferric oxide mineral from reflectance spectroscopy by best-fit matching to standards. With the available data, we consider that both hematite and goethite contributed to diminished reflectance values.

The conclusion that both hematite and goethite are main mineralogic sources of RF bears on the efficacy of snow-radiation models. This conclusion strongly implies that such models can be improved with incorporation of goethite because dust optical properties in most RF models have considered hematite as the only ferric oxide (e.g., Scanza et al., 2015; see Zhang et al., 2015; cf Kaspari et al., 2014). Such usage is reasonable for two reasons. First, optical properties for hematite specimens are available, whereas only a few measurements have been made for goethite (Zhang et al., 2015). Second, soil-mineral maps display hematite, but not goethite, occurrences, noting that Nickovic et al. (2012) sensibly lumped any possible goethite occurrences into a hematite class. As a tangential caution, however, the optical properties used for hematite RF models appear to have been inadequately developed, raising concern about the validity of even the optical properties of hematite, according to Zhang et al. (2015).

The presence of goethite in the ALM DOS samples adds to growing awareness of its widespread occurrences in dust (Arimoto et al., 2002; Alfaro et al., 2004; Lafon et al., 2004, 2006; Lázaro et al., 2011; Mackie et al., 2008; Schroth et al., 2009; Formenti et al., 2010; Maher, 2011; Shi et al., 2011, 2012; Reynolds, Goldstein et al., 2014, Reynolds, Cattle et al., 2014; Zhang et al., 2015; Engelbrecht et al., 2016; Moskowitz et al., 2016; Wu et al., 2016; Lu et al., 2017). The distinction between goethite and hematite may be important because they possess different optical properties at short wavelengths, both in terms of magnitude and spectral dependence (Bedidi & Cervelle, 1993; Lafon et al., 2006). Ultimately, values of complex refractive indices of goethite and hematite, especially the imaginary part that controls their optical absorptions, should be better established in order to improve RF models (Lafon et al., 2006; Zhang et al., 2015).

In a different approach, Skiles and Painter et al. (2018) examined relations between snow optical properties and observed surface reflectance to refine the spectral complex refractive index and single-scattering optical properties of dust deposited on mountain snow. Linking the empirical approach to new knowledge of ferric oxide concentrations, types, sizes, and occurrences might further improve LAP optical properties to refine snow-radiation models.

The possibility that black carbon contributed to diminished snow-cover albedo at the SASP site is implied by the correspondence between relatively low reflectance values and relatively high amounts of organic carbon. The close correspondences between organic carbon and certain trace metals and among these metals further suggest genetic connections to anthropogenic emissions, including those from coal combustion (Nriagu & Pacyna, 1988; Pacyna et al., 1995; Vassilev & Vassilev, 1997; Goldhaber et al., 2004; Ruhl et al., 2009;

Reynolds et al., 2010; Reynolds, Goldstein et al., 2014: Carling et al., 2012; Di Mauro et al., 2019; Figure 8). This interpretation implies that black carbon was a constant proportion of the carbonaceous matter. Examples of such metals include Cs, Cu, Pb, Zn, As, Mo, and Cd that occurred in amounts much greater than their average concentrations in the Upper Continental Crust (Rudnick & Gao, 2003). These results thereby implicate the presence of industrial soot and related effluents in SJM DOS. The observed occurrences of metals in organic particles and coal char support this likelihood. Additional signatures of anthropogenic dust are the correlations among metals, magnetite, and organic carbon. In addition to the presence of magnetite-rich fly ash, anthropogenic magnetite was evident in correlations (r^2 ~0.9) between concentrations of many metals and magnetite measured in certain magnetic properties, such as saturation isothermal magnetization (SIRM) and saturation magnetization (M_s).

Some metals (e.g., Ba, Cd, Cu, Cr, Ni, Pb, Sb, and Zn) are associated with emissions from tailpipes of road motor vehicles and brake wear and are commonly concentrated in the $PM_{2.5}$ fraction at local scales (Chellam et al., 2005; Hulskotte et al., 2007; Lough et al., 2005; Schauer et al., 2006; Smichowski et al., 2008; Thurston et al., 2011; Werkenthin et al., 2014). Our study site was about 0.5 km from and 60 m above U.S. Highway 550, raising the possibility that truck and car emissions contributed to the observed metal loads and perhaps carbon in DOS. These metals bore no positive association with $PM_{2.5}$ (e.g., Figure S11e), a finding consistent with far-traveled metalliferous dust having many sources instead of nearby vehicular traffic on the highway.

Another possible source of organic carbon, soot from wildfire ash, is unlikely, considering the offset in the timing of winter snow accumulation and warm-season regional wildfires. Some unknown proportion of organic carbon, however, was probably derived from local vegetation in fragments too small to be seen and removed on visual examination of the samples. This possibility is supported by the identification of pine pollen in the reflectance spectra of the WY15 ALM sample, which contained the highest amount of organic matter (10 wt.%; Figure S1b). Nevertheless, the correlations of metals with organic carbon strongly suggest that much carbon was associated with regional emissions and not with local vegetation.

The specific effect of black-carbon particles on snow-cover RF in this setting remains uncertain, but our results place limits on the amounts of these particles. If all organic carbon in the ALM samples occurred in soot, taking this unreasonable proposition as an example, then the black-carbon mass in the ALM samples would range about 1.8–9.7 wt.%, using a 0.94 factor to convert the carbon into mass of soot (Chylek et al., 2015). Considering the presence of other types of carbonaceous matter (pollen and other vegetation), black-carbon concentrations must be less.

These results align with those of Skiles and Painter et al. (2018), who estimated that black carbon accounted for no more than 10% of all LAP deposited over the course of WY13, thus implying that such carbon must have had little RF influence. As mentioned in the foregoing, WY13 dust in the ALM sample was dominated by two dust events, both with very high mass loadings, and the WY13 ALM sample contained only 1.9% organic carbon and 2.6% total carbon. These factors may explain low amounts of carbonaceous matter as dilution by extraordinarily large mineral dust input.

Several possibilities might explain why ALM dust mass had strong influence on many properties. The ALM sample with lowest dust loading (WY15) possessed relatively low Rvis and Rtot, along with relatively high HIRM, magnetite amount, organic carbon, and trace-metal concentrations. The sample with highest dust loading (WY13) had opposite relations.

The high concentrations of ferric oxide, magnetite, and metals in the WY15 sample may have resulted largely from "background" dust fall, in the absence of large dust storms that year. If so, the low-mass WY15 sample likely represents dust related to widespread emissions, such as from fugitive and industrial sources, to a greater degree than any other ALM sample. Alternatively, or in conjunction, the relatively high iron oxide abundance in the low-mass WY15 sample may be ascribed—as coincidence—to sources for its three minor dust events that were relatively high in all iron oxide minerals and metals. Under a similar coincidence, the sources for the massive WY13 dust-fall events, especially for D6, were relatively low in ferric oxide and magnetite, rendering the relations shown in Figure 12 as coincidental.

Independent evidence for the presence of background dust is provided by a record of dust deposition as Total Suspended Particulates (TSP) at nearby Telluride (11-km WNW distant at 2,884-m elevation) during parts of

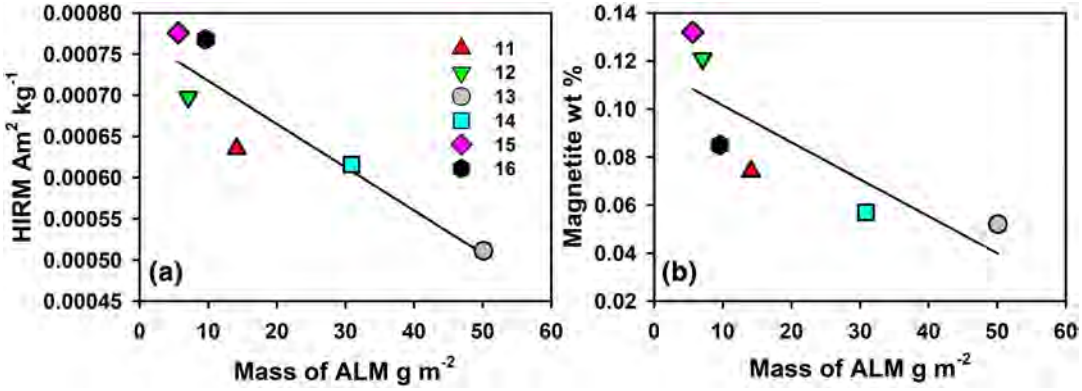

Figure 12. Bivariate plots of (a) ALM mass vs. HIRM ($r^2 = 0.83$, p value = 0.011) and (b) magnetite wt.% (right diagram; $r^2 = 0.41$, p value = 0.167).

WYs 11, 12, and 13. Methods and results of that investigation are described by Reynolds et al. (2016). The TSP filter samples were collected approximately every 2 weeks. We compared TSP dust loads over these periods with times of dust events that resulted in IDLs (http://www.codos.org/; accessed 21 May 2019). Some TSP mass loadings during periods lacking IDLs at SASP were nearly the same as or greater than those during periods of IDL deposition (Table S11). The validity of these comparisons is strengthened by the record of very high TSP mass loading during the 8 April 2013 to 22 April 2013 period that encompassed the WY13 D6 event, the largest such event of record at SASP. Further evidence for important contributions from background dust in snow cover elsewhere is found in trace-element enrichments in Wasatch Range, Utah (Carling et al., 2012).

Similar factors can be invoked to explain the inverse relation between organic carbon and ALM sample mass: The combined effects of (1) continuous or episodic organic carbon deposition onto snow cover during relatively low-dust-mass years, such that organic carbon was concentrated in the resulting ALM layer (e.g., WY15), and (2) an approximately equivalent amount (assumed) of organic matter deposited onto snow cover during a relatively high-dust-mass year such that organic carbon was diluted in that year's ALM layer (WY13). Late-season accumulation of organic matter, especially pollen, may have been similarly concentrated or diluted. It seems less likely that the associations were simply happenstance that the active dust sources during low-dust years were rich in organic carbon and that the active sources during high-dust years were depleted in organic carbon.

An important question remains: Why do many ALM properties vary little compared with the wide ranges in such properties of the IDLs? Two explanations, not mutually exclusive, may be considered. First, the large intraseasonal variations for the IDLs were attenuated (i.e., "averaged-out") by their coalescence to produce each ALM layer, at least with respect to the properties that control RF. Second, background dust inputs might have influenced ALM properties, with degrees of those influences depending on cumulative IDL masses from discrete dust events and storms. Atmospheric scavenging of particles during wet deposition is a likely contributor to background dust fall. As stated in the foregoing, we presume that the low-dust-load ALM WY15 sample represented background dust inputs to the largest extent. Detailed studies of IDLs have produced important understanding about how these DOS layers acquire their properties (e.g., Axson et al., 2016). Nevertheless, we emphasize that ALM compositions are much more representative than those of one or a few IDLs for use in snow-radiation modeling when considering end-of-season snow-melt timing and rates.

The high degree of variance in the compositions of the IDLs indicates that multiple sources produce dust for the SJM because wind storms over deserts in the American West tap different dust sources at different times. Many factors control when and how such sources deliver dust to the SJM: wind-storm strength and direction, availability and PSD of sediment, as well as ecological conditions related to antecedent weather and climatic conditions manifested in vegetation dynamics and soil moisture. In this study, we have not attempted to identify dust sources. The issue of dust sources for SJM and environs has been covered in several recent studies, on the basis of satellite retrievals, back-trajectory analysis, and eye-witness observations (Axson et al., 2016; Neff et al., 2013; Reynolds et al., 2016; Skiles et al., 2015). Such information points generally

to dryland source regions along the Little Colorado River drainage basin (AZ), in the Chinle Valley (AZ, UT), in the Chuska Valley (NM), as well as parts of southeastern and east-central Utah, the Uinta Basin (UT and CO), and the Great Basin of Utah and Nevada.

More work to identify specific recurrent point sources would assist the goal of mitigating emissions, as possible. Our data have revealed some geochemical relations that are irrelevant to RF but that may be important for on-going studies to identify specific point sources (Figure 11). As such, these results can form a foundation on which to detect such locales of recurrent emission, posing, for example, the following questions: Where are the sources for goethite and hematite? What are the types and sources of organic carbon? Why is the WY14 ALM DOS sample unique in its PSDs?

5. Conclusions

Limited research has been done to identify the minerals and other particles in DOS layers that diminish the albedo of snow surfaces and, consequently, advance the timing of snow melt and enhance the rate of melting. Uncertainties persist, moreover, about how such LAPs in these layers vary at a site intraseasonally and interannually. More data on DOS properties, as presented herein, would improve models of RF by dust on snow cover.

Comparisons among reflectance values and physical and chemical properties in DOS layers reveal compositional influences on snow-cover albedo at the SASP site in the SJM of southwestern Colorado. This site is well situated to evaluate how environmental factors, including dust deposited to snow surfaces, influence the rate of snow melt and hence water availability in the Colorado River Basin.

The LAPs that diminished laboratory-measured reflectance in the last yearly sampled DOS layer composed of all dust for water years WY11–16 (the ALM samples) were ferric oxide minerals, dark minerals and rock particles, and forms of organic matter inferred to be black carbon that originated mostly from combustion of fossil fuels. A combination of factors has influenced the amounts of light-absorbing dust constituents: (1) dilution or concentration of LAPs in ALM dust, depending on relatively more or less (respectively) total dust load from dust events and storms, and (2) varying contributions from different dust-source sediments having originally low or high amounts of the influential dust constituents. During WY15, very little dust was deposited in discrete dust-event layers, such that the WY15 ALM sample, more than others, represented regional, background dust fall. Relative to masses of all ALM samples (in g m^{-2}), the WY15 sample contained more iron oxide minerals, organic carbon, and metals, all of which were highly correlated.

The ferric oxide minerals were hematite, mostly microcrystalline, and goethite, mostly nano-size. On the basis of Mössbauer spectroscopy, amounts of hematite plus goethite ranged 1.4–1.8 wt.% of bulk ALM samples. These results can inform RF models when optical properties for the sizes and occurrences of these minerals are determined. Importantly, we found that the ferric oxide minerals commonly occurred in and on mineral-aggregated, silt-size particles (commonly >4 μm), as documented elsewhere (Moskowitz et al., 2016; Reynolds, Cattle et al., 2014; Reynolds, Goldstein et al., 2014). These observations may prompt adjustments to current snow-melt models that limit particle sizes at <6 μm to simulate surface-dust deposition at regional scales (e.g., Oaida et al., 2015).

The correspondence between reflectance and magnetite abundance suggests that magnetite is a surrogate for DRPs and minerals (e.g., pyroxenes and amphiboles) that presumably can diminish reflectance. The presence of very fine-grained magnetite inside silt-size DRPs implies that small, but easily measured, amounts of magnetite can be used to extrapolate to the relatively large surface areas of LAPs. Tests of this proposition might reveal that DRPs are a missing component in determining RF from dust at SASP and elsewhere, including in the atmosphere.

Iron-bearing minerals are clearly important dust constituents for their potential effects on RF in the atmosphere and on snow cover, as well as on many other environments. For this reason, the presence and amount of Fe in dust has been found or reasonably considered to be an indirect measure for dust concentrations and (or) the influence of iron-bearing minerals on RF (Axson et al., 2016; Derimian et al., 2008; Di Mauro et al., 2019; Kaspari et al., 2014; Moosmüller et al., 2012). In the ALM samples, ironically, Fe concentrations were not directly correlated with reflectance values nor with Fe-bearing minerals that affect reflectance. Instead, iron had strong affinity with Al in the clay fraction. In this setting, therefore, Fe concentrations

are not a reliable surrogate for determining whether or how Fe oxide minerals might influence RF. Iron concentrations by themselves should be applied cautiously in other settings.

Low amounts of organic carbon indicate that concentrations of black carbon did not exceed a few weight percent in five of six ALM samples. The highest concentration of organic carbon was found the WY15 ALM sample, which contained abundant pollen. This sample exhibited lowest reflectance values and the highest levels of iron oxide minerals. The close associations between organic carbon and contaminant trace metals strongly suggest the presence of black carbon produced by fossil-fuel combustion from industrial activities and transportation far from the SASP site.

Summarizing the contributions of the LAPs in the DOS samples to potential albedo effects, the ferric oxide minerals were spectrally dominant, and their amounts corresponded closely to diminished laboratory-measured reflectance. With respect to dark particles, we did not observe the diagnostic broad absorption features of dark minerals in reflectance spectra. Nevertheless, the amounts of such dark minerals and rock particles, as inferred from magnetite concentration, also corresponded negatively with reflectance presumably by lowering reflectance in the visible to short wavelength infrared. The specific RF effects of black carbon at this site were likely variable and small, and they remain an open question because of the large range in organic carbon and complications from the presence of pollen.

Our findings likely represent the range of dust-layer properties on SJM snow cover over more than a few years because source areas for these dust layers will likely be active over the near future, on the order of years. With respect to dust radiative properties, our findings are limited to SJM snow cover. Other montane settings in the American West are affected by dust from many regional sources, some of which are far separated and geologically different from those for SJM dust layers (Carling et al., 2012; Dastrup et al., 2018; Hahnenberger & Nicoll, 2012, 2014; Miller et al., 2012; Munroe et al., 2019; Reynolds, Goldstein et al., 2014). Analyses of DOS from other areas would help evaluate the influences of varied dust sources, climate, wind-storm patterns, and anthropogenic inputs on snow melt and water resources in and beyond the Colorado River Basin.

During the next few decades, compositions of future DOS layers might change because of anticipated changes in the landscape and climate in dust-source regions, such as vegetation change in response to warming and drying, along with human-related disturbances and even expansion of drylands vulnerable to wind erosion (Achakulwisut et al., 2018; Duniway et al., 2019; Munson et al., 2011; Seager et al., 2007). These possibilities indicate the importance of continued measurement of DOS compositions for contributions to modeling in support of water-management strategies as well as for signals of landscape change.

Acknowledgments
Authors declare no real or perceived financial conflicts of interests or other affiliations that may be construed as having a conflict of interest with respect to the results of this paper. The data supporting the conclusions can be obtained in Supporting Information S1 and in the ScienceBase database, https://doi.org/10.5066/P9RGQ9KX (Reynolds et al., 20202020). We thank Mike Duniway and two anonymous reviewers for improving the manuscript. We are grateful to Michael Sirles for providing the carbon analyses, Chris Landry and Andrew Temple for sample collection 2011–2015, and Jeremy Havens for preparation of Figure 11. Mention of trade names is for information purposes only and does not imply endorsement by the U.S. Geological Survey. This study was supported by the Land Change Science Program of the U.S. Geological Survey. The Institute for Rock Magnetism is supported by a grant EAR-1642268 from the Instruments and Facilities Program, Division of Earth Science, National Science Foundation. This is IRM contribution 1904.

References

Achakulwisut, P., Mickley, L. J., & Anenberg, S. C. (2018). Drought-sensitivity of fine dust in the U.S. Southwest: Implications for air quality and public health under future climate change. *Environmental Research Letters*, *13*. https://doi.org/10.1002/2017JD027208

Alfaro, S. C., Lafon, S., Rajot, J. L., Formenti, P., Gaudichet, A., & Maille, M. (2004). Iron oxides and light absorption by pure desert dust: An experimental study. *Journal of Geophysical Research*, *109*, D08208. https://doi.org/10.1029/2003JD004374

Arimoto, R., Balsam, W., & Schloesslin, C. (2002). Visible spectroscopy of aerosol particles collected on filters: Iron oxide minerals. *Atmospheric Environment*, *36*, 89–96.

Axson, J. L., Shen, H., Bondy, A. L., Landry, C. C., Welz, J., Creamean, J. M., & Ault, A. P. (2016). Transported mineral dust deposition case study at a hydrologically sensitive mountain site: Size and composition shifts in ambient aerosol and snowpack. *Aerosol and Air Quality Research*, *16*(555–567), 2016. https://doi.org/10.4209/aaqr.2015.05.0346

Bedidi, A., & Cervelle, B. (1993). Light scattering by spherical particles with hematite and goethite like optical properties: Effect of water impregnation. *Journal of Geophysical Research*, *98*(B7), 11,941–11,952. https://doi.org/10.1029/93JB00188

BBerquó, T. S., Imbernon, R. A. L., Blot, A., Franco, D. R., Toledo, M. C. M., & Partiti, C. S. M. (2007). Low temperature magnetism and Mössbauer spectroscopy study from natural goethite. *Physics and Chemistry of Minerals*, *34*(5), 287–294. https://doi.org/10.1007/s00269-007-0147-9

Bond, T. C., & Bergstrom, R. W. (2006). Light absorption by carbonaceous particles: An investigative review. *Aerosol Science and Technology*, *40*(1), 27–67.

Bond, T. C., Doherty, S. J., Fahey, D. W., Forster, P. M., Berntsen, T., DeAngelo, B. J., et al. (2013). Bounding the role of black carbon in the climate system: A scientific assessment. *Journal of Geophysical Research: Atmospheres*, *118*, 5380–5552. https://doi.org/10.1002/jgrd.50171

Briggs, P. H. (2002). The determination of forty elements in geological and botanical samples by inductively coupled plasma-atomic emission spectrometry. In: Taggart Jr., J.E. (Ed.), Analytical Methods for Chemical Analysis of Geologic and Other Materials, pp. I1eI14. U.S. Geological Survey Open-File Report 02e223.

Briggs, P. H., & Meier, A. L. (2002). The determination of forty-two elements in geological materials by inductively coupled plasma-mass spectrometry. In: Taggart Jr., J.E. (Ed.), Analytical Methods for Chemical Analysis of Geologic and Other Materials, pp. I1eI14. U.S. Geological Survey Open-File Report 02-223.

Carling, G. T., Fernandez, D. P., & Johnson, W. P. (2012). Dust-mediated loading of trace and major elements to Wasatch Mountain snowpack. *Science of the Total Environment*, *432*, 65–77.

Chellam, S., Kulkarni, P., & Fraser, M. P. (2005). Emissions of organic compounds and trace metals in fine particulate matter from motor vehicles: A tunnel study in Houston, Texas. *Journal of the Air and Waste Management Association*, *55*(1), 60–72. https://doi.org/10.1080/10473289.2005.10464597

Chylek, P., Jennings, S. G., & Pinnck, R. (2015). AERSOLS|Soot. *Encyclopedia of Atmospheric Sciences (Second Edition)*, *2015*, 86–91. https://doi.org/10.1016/B978-0-12-382225-3.00375-3

Clark, R. N., Swayze, G. A., Wise, R. A., Livo, K. E., Hoefen, T. M, Kokaly, R. F., and Sutley, S.J. (2007). USGS digital spectral library splib06a: U.S. Geological Survey Data Series 231, http://speclab.cr.usgs.gov/spectral.lib06/ds231/index.html.

Clow, D. W., & Ingersoll, G. I. (1994). Particulate carbonate matter in snow from selected sites in the south-central Rocky Mountains. *Atmospheric Environment*, *28*, 575–584.

Clow, D. W., Williams, M. W., & Schuster, P. W. (2016). Increasing aeolian dust deposition to snowpacks in the Rocky Mountains inferred from snowpack, wet deposition, and aerosol chemistry. *Atmospheric Environment*, *146*, 183–194. https://doi.org/10.1016/j.atmosenv.2016.06.076

Dang, C., & Hegg, D. A. (2014). Quantifying light absorption by organic carbon in western North American snow by serial chemical extractions. *Journal of Geophysical Research: Atmospheres*, *119*, 10,247–10,261. https://doi.org/10.1002/2014JD022156

Dang, C., Warren, S. G., Fu, Q., Doherty, S. J., Sturm, M., & Su, J. (2017). Measurements of light-absorbing particles in snow across the Arctic, North America, and China: Effects on surface albedo. *Journal of Geophysical Research: Atmospheres*, *122*, 10,149–10,168. https://doi.org/10.1002/2017JD027070

Dastrup, D. B., Carling, G. T., Collins, S. A., Nelson, S. T., Fernandez, D. P., Tingey, D. G., et al. (2018). Aeolian dust chemistry and bacterial communities in snow are unique to airshed locations across northern Utah, USA. *Atmospheric Environment*, *193*, 251–261. https://doi.org/10.1016/j.atmosenv.2018.09.016

Deems, J., Painter, T. H., Barsugli, J., Belnap, J., & Udall, B. (2013). Combined impacts of current and future dust deposition and regional warming on Colorado River Basin snow dynamics and hydrology. *Hydrology and Earth System Sciences*, *17*.

Derbyshire, E. (2007). Natural minerogenic dust and human health. *Ambio: A Journal of the Human Environment*, *36*(1), 73–77. https://doi.org/10.1579/0044-7447(2007

Derimian, Y., Karnieli, A., Kaufman, Y. J., Andreae, M. O., Andreae, T. W., Dubovik, O., et al. (2008). The role of iron and black carbon in aerosol light absorption. *Atmospheric Chemistry and Physics*, *8*, 3623–3637. https://doi.org/10.5194/acp-8-3623-2008

Di Mauro, B., Garzonio, R., Rossini, M., Filippa, G., Pogliotti, P., Galvagn, M., et al. (2019). Saharan dust events in the European Alps: Role in snowmelt and geochemical characterization. *The Cryosphere*, *13*(4), 1147–1165. https://doi.org/10.5194/tc-13-1147-2019

Doherty, S. J., Dang, C., Hegg, D. A., Zhang, R., & Warren, S. G. (2014). Black carbon and other light-absorbing particles in snow of central North America. *Journal of Geophysical Research: Atmospheres*, *119*, 12,807–12,831. https://doi.org/10.1002/2014JD022350

Duniway, M. C., Pfennigwerth, A., Fick, S. E., Nauman, T. W., Belnap, J., & Barger, N. N. (2019). Wind erosion and dust from US drylands: A review of causes, consequences, and solutions in a changing world. *Ecosphere*, *10*(3), e02650. https://doi.org/10.1002/ecs2.2650

Dunlop, D. J. (2002). Theory and application of the Day plot (Mrs/Ms v. Hcr/Hc). 1. Theoretical curves and tests using titanomagnetite data. *Journal of Geophysical Research*, *107*(B3), 2057. https://doi.org/10.1029/2001JB000487

Engelbrecht, J. P., Moosmüller, H., Pincock, S., Jayanty, R. K. M., Lersch, T., & Casuccio, G. (2016). Technical note: Mineralogical, chemical, morphological, and optical interrelationships of mineral dust re-suspensions. *Atmospheric Chemistry and Physics*, *16*, 10,809–10,830. https://doi.org/10.5194/acp-16-10809-2016

Evans, M. E., & Heller, F. (2003). *Environmental magnetism: Principles and applications of enviromagnetics*. London: Academic Press.

Field, J. P., Belnap, J., Breshears, D. D., Neff, J. C., Okin, G. S., Whicker, J. J., et al. (2009). The ecology of dust. *Frontiers in Ecology and the Environment*, *8*(8), 423–430. https://doi.org/10.1890/090050

Flanders, P. J. (1999). Identifying fly ash at a distance from fossil fuel power stations. *Environmental Science & Technol*, *33*, 528–532.

Flanner, M. G., Liu, X., Zhou, C., Penner, J. E., & Jiao, C. (2012). Enhanced solar energy absorption by internally-mixed black carbon in snow grains. *Atmospheric Chemistry and Physics*, *12*, 4699–4721. https://doi.org/10.5194/acp-12-4699-2012

Flanner, M. G., Zender, C. S., Hess, P. G., Mahowald, N. M., Painter, T. H., Ramanathan, V., & Rasch, P. J. (2009). Springtime warming and reduced snow cover from carbonaceous particles. *Atmospheric Chemistry and Physics*, *9*, 2481–2497. https://doi.org/10.5194/acp-9-2481-2009

Flanner, M. G., Zender, C. S., Randerson, J. T., & Rasch, P. J. (2007). Present-day climate forcing and response from black carbon in snow. *Journal of Geophysical Research*, *112*, D11202. https://doi.org/10.1029/2006JD008003

Formenti, P., Schuetz, L., Balkanski, Y., Desboeufs, K., Ebert, M., Kandler, K., et al. (2010). Recent progress in understanding physical and chemical properties of mineral dust. *Atmospheric Chemistry and Physics Discussions*, *10*, 31,187–31,251. https://doi.org/10.5194/acpd-10-31187

Gassó, S., Grassian, V. H., & Miller, R. L. (2010). Interactions between mineral dust, climate, and ocean ecosystems. *Elements*, *6*, 247–252.

Gieré, R., & Querol, X. (2010). Solid particulate matter in the atmosphere. *Elements*, *6*, 215–222.

Ginot, P., Dumont, M., Lim, S., Patris, N., Taupin, J.-D., Wagnon, P., et al. (2014). A 10 year record of black carbon and dust from a Mera Peak ice core (Nepal): Variability and potential impact on melting of Himalayan glaciers. *The Cryosphere*, *8*, 1479–1496. https://doi.org/10.5194/tc-8-1479-2014

Goldhaber, M. B., Callender, E., & Reynolds, R. L. (2004). The geochemical and magnetic record of coal-combustion products in West Virginia reservoir sediments and soils. In R. J. Hill, J. Leventhal, Z. Aizenshtat, M. J. Baedecker, G. Claypool, R. Eganhouse, M. Goldhaber, & K. Peters (Eds.), *Geochemical investigations in earth and space science* (pp. 159–186). Amsterdam: The Geochemical Society, Publication.

Goudie, A. S., & Middleton, N. J. (2006). *Desert dust in the global system* (p. 287). Berlin: Springer.

Guyodo, Y., LaPara, T. M., Anschutz, A. J., Penn, R. L., Banerjee, S. K., Geiss, C. E., & Zanner, W. (2006). Rock magnetic, chemical and bacterial community analysis of a modern soil from Nebraska. *Earth and Planetary Science Letters*, *251*(1–2), 168–178.

Hadley, O., & Kirschstetter, T. W. (2012). Black-carbon reduction of snow albedo. *Nature Climate Change*, *2*, 437–440. https://doi.org/10.1038/nclimate1433

Hadley, O. L., Corrigan, C. E., Kirchstetter, T. W., Cliff, S. S., & Ramanathan, V. (2010). Measured black carbon deposition on the Sierra Nevada snow pack and implication for snow pack retreat. *Atmospheric Chemistry and Physics.*, *10*, 7505–7513. https://doi.org/10.5194/acpd-10-7505-2010

Hahnenberger, M., & Nicoll, K. (2012). Meteorological characteristics of dust transport events in the eastern Great Basin of Utah, USA. *Atmospheric Environment*, *60*, 601–612. https://doi.org/10.1016/j.atmosenv.2012.06.029

Hahnenberger, M., & Nicoll, K. (2014). Geomorphic and land cover identification of dust sources in the eastern Great Basin of Utah, U.S.A. *Geomorphology*, *204*, 657–672. https://doi.org/10.1016/j.geomorph.2013.09.013

Hansen, J., & Nazarenko, L. (2004). Soot climate forcing via snow and ice albedos. *Proceedings of the National Academy of Sciences*, *101*(2), 423–428. https://doi.org/10.1073/pnas.2237157100

Hulskotte, J. H. J., van der Gon, H. A., Denier, C., Visschedijk, A. J. H., & Schaap, M. (2007). Brake wear from vehicles as an important source of diffuse copper pollution. *Water Science and Technology*, *56*(1), 223–231. https://doi.org/10.2166/wst.2007.456

Jackson, M., & Solheid, P. (2010). On the quantitative analysis and evaluation of magnetic hysteresis data. *Geochemistry Geophysics Geosystems*, *11*, Q04Z15. https://doi.org/10.1029/2009GC002932

Jickells, T. D., An, Z. S., Andersen, K. K., Baker, A. R., Bergametti, G., Brooks, N., et al. (2005). Global iron connections between desert dust, ocean biogeochemistry, and climate. *Science*, *308*(5718), 67–71. https://doi.org/10.1126/science.1105959

Kaspari, S., Painter, T. H., Gysel, M., Skiles, S. M., & Schwikowski, M. (2014). Seasonal and elevational variations of black carbon and dust in snow and ice in the Solu-Khumbu, Nepal and estimated radiative forcings. *Atmospheric Chemistry and Physics*, *14*, 8089–8103. https://doi.org/10.5194/acp-14-8089-2014

Kaufman, Y. J., Tanré, D., Dubovik, O., Karnieli, A., & Remer, L. A. (2001). Absorption of sunlight by dust as inferred from satellite and ground-based remote sensing. *Geophysical Research Letters*, *28*(8), 1479–1482.

Knippertz, P., & Stuut, J. B. W. (2014). *Mineral dust: A key player in the Earth system* (p. 509). Dordrecht, Netherlands: Springer. https://doi.org/10.1007/978-94-017-8978-3

Kokaly, R. F. (2011). PRISM—Processing routines in IDL for spectroscopic measurements (installation manual and user's guide, version 1.0): U.S. Geological Survey Open-File Report 2011–1155, 431 p. http://pubs.usgs.gov/of/2011/1155/

Lafon, S., Rajot, J. L., Alfaro, S. C., & Gaudichet, A. (2004). Assessing the iron-oxides content in desert aerosols. *Atmospheric Environment*, *38*(8), 1211–1218.

Lafon, S., Sokolik, I. N., Rajot, J. L., Caquineau, S., & Gaudichet, A. (2006). Characterization of iron oxides in mineral dust aerosols: Implications for light absorption. *Journal of Geophysical Research*, *111*, D21207. https://doi.org/10.1029/2005JD007016

Landry, C. C., Buck, K., Raleigh, M. S., & Clark, M. P. (2014). Mountain system monitoring at senator Beck Basin, San Juan Mountains, Colorado: a new integrative data source to develop and evaluate models snow and hydrologic processes. *Water Resources Research*, *50*, 1773–1788. https://doi.org/10.1002/2013WR013711

Lauf, R. J. (1982). Microscructures of coal fly ash particles. *Ceramics Bulletin*, *61*, 487–490.

Lawrence, C. R., Painter, T. H., Landry, C. C., & Neff, J. C. (2010). Contemporary geochemical composition and flux of aeolian dust to the San Juan Mountains, Colorado, United States. *Journal of Geophysical Research*, *115*, G03007. https://doi.org/10.1029/2009JG001077

Lawrence, C. R., Reynolds, R. L., Ketterer, M., & Neff, J. C. (2013). Aeolian controls on soil geochemistry and weathering fluxes in high-elevation ecosystems of the Rocky Mountains, USA. *Geochimica et Cosmochimica Acta*, *107*, 27–46.

Lázaro, F. J., Gutiérrez, L., Barrón, V., & Gelado, M. D. (2011). The speciation of iron in desert dust collected in Gran Canaria (Canary Islands): Combined chemical, magnetic and optical analysis. *Atmospheric Environment*, *42*, 8987–8996. https://doi.org/10.1016/j.atmosenv.2008.09.035

Locke, G., & Bertine, K. K. (1986). Magnetite in sediments as an indicator of coal combustion. *Applied Geochemistry*, *50*, 345–356.

Lough, G. C., Schauer, J. J., Park, J.-S., Shafer, M. M., DeMinter, J. T., & Weinstein, J. P. (2005). Emissions of metals associated with motor vehicle roadways. *Environmental Science & Technolnology*, *39*(3), 826–836. https://doi.org/10.1021/es048715f

Lu, W., Zhao, W., Balsam, W., Lu, H., Liu, P., Lu, Z., & Ji, J. (2017). Iron mineralogy and speciation in clay-sized fractions of Chinese desert sediments. *Journal of Geophysical Research: Atmospheres*, *122*, 13,458–13,471. https://doi.org/10.1002/2017JD027733

Mackie, D. S., Boyd, P. W., McTainsh, G. H., Tindale, N. W., Westberry, T. K., & Hunter, K. A. (2008). Biogeochemistry of iron in Australian dust: From eolian uplift to marine uptake. *Geochemistry, Geophysics, Geosystems*, *9*, Q03Q08. https://doi.org/10.1029/2007GC001813

Maher, B. A. (2011). The magnetic properties of quaternary aeolian dusts and sediments, and their paleoclimatic significance. *Aeolian Research*, *3*, 87–144. https://doi.org/10.1016/j.aeolia.2011.01.005

Maher, B. A., Prospero, J. M., Mackie, D., Gaiero, D., Hesse, P. P., & Balkanski, Y. (2010). Global connections between aeolian dust, climate, and ocean biogeochemistry at the present day and at the last glacial maximum. *Earth-Science Reviews*, *99*(1-2), 61–97. https://doi.org/10.1016/j.earscirev.200912.001

Mahowald, N. M., Kloster, S., Engelstaedter, S., Moore, J. K., Mukhopadhyay, S., McConnell, J. R., et al. (2010). Observed 20th century desert dust variability: Impact on climate and biogeochemistry. *Atmospheric Chemistry and Physics*, *10*, 10,875–10,893. https://doi.org/10.5194/acp-10-10875-2010

Miller, M. E., Bowker, M. A., Reynolds, R. L., & Goldstein, H. L. (2012). Post-fire land treatments and wind erosion—Lessons from the Milford Flat Fire, UT, USA. *Aeolian Research*, *7*, 29–44. https://doi.org/10.1016/j.aeolia.2012.04.001

Moosmüller, H., Engelbrecht, J. P., Skiba, M., Frey, G., Chakrabarty, R. K., & Arnott, W. P. (2012). Single scattering albedo of fine mineral dust aerosols controlled by iron concentration. *Journal of Geophysical Research*, *117*, D11210. https://doi.org/10.1029/2011JD01690

Moskowitz, B. M., Reynolds, R. L., Goldstein, H. L., Berquó, T. S., Kokaly, R. F., & Bristow, C. S. (2016). Iron oxide minerals in dust-source sediments from the Bodélé Depression, Chad. Implications for radiative properties and Fe bioavailability of dust plumes from the Sahara. *Aeolian Research*, *22*, 93–206.

Munroe, J. S., Norris, E. D., Carling, G. T., Beard, B. L., Satkoski, A. M., & Liu, L. (2019). Isotope fingerprinting reveals western North American sources of modern dust in the Uinta Mountains, Utah, USA. *Aeolian Research*, *38*, 39–47. https://doi.org/10.1016/j.aeolia.2019.03.005

Munson, S. M., Belnap, J., & Okin, G. S. (2011). Responses of wind erosion to climate-induced vegetation changes on the Colorado Plateau. *Proceedings of the National Academy of Sciences USA*, *108*, 3854–3859.

Nagorski, S. A., Kaspari, S. D., Hood, E., Fellman, J. B., & Skiles, S. M. (2019). Radiative forcing by dust and black carbon on the Juneau Icefield, Alaska. *Journal of Geophysical Research: Atmospheres*, *124*, 3943–3959. https://doi.org/10.1029/2018JD029411

Neff, J. C., Ballantyne, A. P., Farmer, G. L.,, Mahowald, N. M., Conroy, J. L., Landry, C. C., et al. (2008). Increasing eolian dust deposition in the western United States linkedto human activity. *Nature Geoscience*, *1*, 189–195. https://doi.org/10.1038/ngeo133

Neff, J. C., Reynolds, R. L., Munson, S., Fernandez, D., & Belnap, J. (2013). The role of dust storms in atmospheric particle concentrations at two sites in the western U.S. *Journal of Geophysical Research: Atmospheres*, *118*, 11,201–11,212. https://doi.org/10.1002/jgrd.50855

Nickovic, S., Vukovic, A., Vujadinovic, M., Djurdjevic, V., & Pejanovic, G. (2012). Technical note: High-resolution mineralogical database of dust-productive soils for atmospheric dust modeling. *Atmospheric Chemistry and Physics*, *12*(845–855), 2012. https://doi.org/10.5194/acp-12-845-2012

Nriagu, J. O., & Pacyna, J. M. (1988). Quantitative assessment of worldwide contamination of air, water, and soils by trace metals. *Nature*, *333*(6169), 134–139.

Oaida, C. M., Xue, Y., Flanner, M. G., Skiles, S. M., De Sales, F., & Painter, T. H. (2015). Improving snow albedo processes in WRF/SSiB regional climate model to assess impact of dust and black carbon in snow on surface energy balance and hydrology over western U.S. *Journal of Geophysical Research: Atmospheres*, *120*, 3228–3248. https://doi.org/10.1002/2014JD022444

Oksanen, J., Blanchet, F. G., Friendly, M., Kindt, R., Legendre, P., McGlinn, D., et al. (2019). Vegan: Community ecology package. R package version 2.5–5. https://CRAN.R-project.org/package=vegan

Özdemir, Ö., & Dunlop, D. J. (2010). Hallmarks of maghemitization in low-temperature remanence cycling of partially oxidized magnetite nanoparticles. *Journal of Geophysical Research*, *115*, B02101. https://doi.org/10.1029/2009JB006756

Pacyna, J. M., Scholtz, M. T., & Li, Y.-F. (1995). Global budget of trace metal sources. *Environmental Reviews*, *3*, 145–159.

Painter, T. H., Barrett, A. P., Landry, C. C., Neff, J. C., Cassidy, M. P., Lawrence, C. R., et al. (2007). Impact of disturbed desert soils on duration of mountain snow cover. *Geophysical Research Letters*, *34*, L12502. https://doi.org/10.1029/2007GL030284

Painter, T. H., Bryant, A., & Skiles, S. M. (2012). Radiative forcing by light absorbing impurities in snow from MODIS surface reflectance data. *Geophysical Research Letters*, *39*, L17502. https://doi.org/10.1029/2012GL052457

Painter, T. H., Deems, J. S., Belnap, J., Hamlet, A. F., Landry, C. C., & Udall, B. (2010). Response of Colorado River runoff to dust radiative forcing in snow. *Proceedings of the National Academy of Sciences USA*, *107*(40), 17,125–17,130. https://doi.org/10.1073/pnas.0913139107

Painter, T. H., Skiles, S. M., Deems, J., Bryant, A., & Landry, C. C. (2012). Dust radiative forcing in snow of the Upper Colorado River Basin: Part 1. A 6 year record of energy balance, radiation, and dust concentrations. *Water Resources Research*, *48*, W07521. https://doi.org/10.1029/2012WR011985

Painter, T. H., Skiles, S. M., Deems, J. S., Brandt, W. T., & Dozier, J. (2018). Variation in rising limb of Colorado River snowmelt runoff hydrograph controlled by dust radiative forcing in snow. *Geophysical Research Letters*, *45*, 797–808. https://doi.org/10.1002/2017GL075826

Qian, Y., Yasunari, T. J., Doherty, S. J., Flanner, M. G., Lau, W. K. M., Ming, J., et al. (2015). Light-absorbing particles in snow and ice: Measurement and modeling of climatic and hydrological impact. *Advances in Atmospheric Sciences*, *32*(1), 64–91. https://doi.org/10.1007/s00376-014-0010-0

Ramanathan, V., & Carmichael, G. (2008). Global and regional climate changes due to black carbon. *Nature Geoscience*, *1*, 221–227. https://doi.org/10.1038/ngeo156

Ramanathan, V., Ramana, M. V., Roberts, G., Kim, D., Corrigan, C., Chung, C., & Winker, D. (2007). Warming trends in Asia amplified by brown cloud solar absorption. *Nature*, *448*(7153), 575–578. https://doi.org/10.1038/nature06019

Redmond, H. E., Dial, K. D., & Thompson, J. E. (2010). Light scattering and absorption by wind-blown dust: Theory, measurement, and recent data. *Aeolian Research*, *2*(5–26), 2010.

Reynolds, R. L., Cattle, S. R., Moskowitz, B. M., Goldstein, H. L., Yauk, K., Flagg, C., et al. (2014). Iron oxide minerals in dust of the Red Dawn event in eastern Australia, September 2009. *Aeolian Research*, *15*, 1–13. https://doi.org/10.1016/j.aeolia.2014.02.003

Reynolds, R. L., Goldstein, H. L., Moskowitz, B. M., Bryant, A. C., Skiles, S. M., Kokaly, R. F., et al. (2014). Composition of dust deposited to snow cover in the Wasatch Range (Utah, USA). Controls on radiative properties of snow cover and comparison to some dust-source sediments. *Aeolian Research*, *15*, 73–90.

Reynolds, R. L., Goldstein, H. L., Moskowitz, B. M., Kokaly, R. F., Munson, S. M., Solheid, P., et al. (2020). Data for Dust deposited on snow cover in the San Juan Mountains, Colorado, 2011–2016: Compositional variability bearing on snow-melt effects. U.S. Geological Survey data release. https://doi.org/10.5066/P9RGQ9KX

Reynolds, R. L., Mordecai, J., Rosenbaum, J., Ketterer, M. E., Walsh, M. K., & Moser, K. (2010). Compositional changes in sediments of subalpine lakes, Uinta Mountains, Utah: Evidence for the effects of human activity on atmospheric dust inputs. *Journal of Paleolimnology*, *44*(1), 161–175. https://doi.org/10.1007/s10933-009-9394-8

Reynolds, R. L., Munson, S. M., Fernandez, D. P., & Neff, J. C. (2016). Concentrations of mineral aerosol from desert to plains across the central Rocky Mountains, western United States. *Aeolian Research*, *23*, 21–35. https://doi.org/10.1016/j.aeolia.2016.09.001

Reynolds, R. L., Sweetkind, D. S., & Axford, Y. (2001). An inexpensive magnetic mineral separator for fine-grained sediment. U.S. Geological Survey Open-file Report 01-281, 7 p.

Rudnick, R. L., & Gao, S. (2003). Composition of the continental crust. In H. D. Holland & K. K. Turekian (Eds.), *Treatise on geochemistry 659* (Vol. 3, pp. 1–64). Amsterdam: Elsevier. https://doi.org/10.1016/B0-08-043751-6/03016-4

Ruhl, L., Vengosh, A., Dwyer, G. S., Hsu-Kim, H., Deonarine, A., Bergin, M., & Kravchenko, J. (2009). Survey of the potential environmental and health impacts in the immediate aftermath of the coal ash spill in Kingston, Tennessee. *Environmental Science & Technolnology*, *43*, 6326–6333.

Scanza, R. A., Mahowald, N., Ghan, S., Zender, C. S., Kok, J. F., Liu, X., et al. (2015). Modeling dust as component minerals in the community atmosphere model: Development of framework and impact on radiative forcing. *Atmospheric Chemistry and Physics*, *15*, 537–561. https://doi.org/10.5194/acp-15-537-2015

Schauer, J. J., Lough, G. C., Shafer, M. M., Christensen, W. F., Arndt, M. F., DeMinter, J. T., & Park, J. S. (2006). Characterization of metals emitted from motor vehicles. *Research Report, Health Effects Institute*, *2006*(133), 1–76. discussion 77-88

Schroth, A. W., Crusius, J., Sholkovitz, E. R., & Bostick, B. C. (2009). Iron solubility driven by speciation in dust sources to the ocean. *Nature Geoscience*, *2*, 337–340.

Seager, R., Ting, M., Held, I., Kushnir, Y., Lu, J., Vecchi, G., et al. (2007). Model projections of an imminent transition to a more arid climate in southwestern North America. *Science*, *316*(5828), 1181–1184. https://doi.org/10.1126/science.1139601

Shao, Y., Wyrwoll, K. H., Chappell, A., Huang, J., Lin, Z., McTainsh, G. . H., et al. (2011). Dust cycle: An emerging core theme in Earth system science. *Aeolian Research*, *2*, 181–204. https://doi.org/10.1016/J.AEOLIA.2011.01.001

Shi, Z., Krom, M. D., Bonneville, S., Baker, A. R., Bristow, C., Drake, N., et al. (2011). Influence of chemical weathering and aging of iron oxides on the potential iron solubility of Saharan dust during simulated atmospheric processing. *Global Biogeochemical Cycles*, *25*, GB2010. https://doi.org/10.1029/2010GB003837

Shi, Z., Krom, M. D., Jickells, T. D., Bonneville, S., Carslaw, K. S., Mihalopoulos, N., et al. (2012). Impacts on iron solubility in the mineral dust by processes in the source region and the atmosphere: A review. *Aeolian Research*, *5*, 21–42. https://doi.org/10.1016/j.aeolia.2012.03.001

Skiles, S. M., Painter, T., & Okin, G. S. (2017). A method to retrieve the spectral complex refractive index and single scattering optical properties of dust deposited in mountain snow. *Journal of Glaciology*, *63*(237), 133–147. https://doi.org/10.1017/jog.2016.126

Skiles, S. M., & Painter, T. H. (2016). A nine-year record of dust on snow in the Colorado River Basin. Proceedings of the 12th Biennial Conference of Research on the Colorado Plateau, Chapter B, Ralston, B.E., (ed.) U.S. Geological Survey Scientific Investigations Report 2015–5180, 11 pp. https://doi.org/10.3133/sir20155180

Skiles, S. M., & Painter, T. H. (2017). Daily evolution in dust and black carbon content, snow grain size, and snow albedo during snowmelt, Rocky Mountains, Colorado. *Journal of Glaciology*, *63*, 118–132. https://doi.org/10.1017/jog.2016.125

Skiles, S. M., & Painter, T. H. (2018). Assessment of radiative forcing by light-absorbing particles in snow from in situ observations with radiative transfer modeling. *Journal of Hydrometeorology*, *19*, 1397–1409. https://doi.org/10.1175/JHM-D-18-0072.1

Skiles, S. M., Painter, T. H., Belnap, J., Holland, L., Reynolds, R. L., Goldstein, H. L., & Lin, J. (2015). Regional variability in dust-on-snow processes and impacts in the Upper Colorado River Basin. *Hydrological Processes*, *29*(26), 5397–5413. https://doi.org/10.1002/hyp.10569

Skiles, S. M., Painter, T. H., Deems, J., Landry, C., & Bryant, A. (2012). Dust radiative forcing in snow of the Upper Colorado River Basin: Part II. Interannual variability in radiative forcing and snowmelt rates. *Water Resources Research*, *48*, W07522. https://doi.org/10.1029/2012WR011986

Smichowski, P., Gómez, D., Frazzoli, C., & Caroli, S. (2008). Traffic-related elements in airborne particulate matter. *Applied Spectroscopy Reviews*, *43*(1), 23–49.

Sokolik, I. N., & Toon, O. B. (1999). Incorporation of mineralogical composition into models of the radiative properties of mineral aerosol from UV to IR wavelengths. *Journal of Geophysical Research*, *104*(D8), 9423–9444. https://doi.org/10.1029/1998JD200048

Sokolik, I. N., Winker, D. M., Bergametti, G., Gillette, D. A., Carmichael, G., Kaufman, Y. J., et al. (2001). Introduction to special section: Outstanding problems in quantifying the radiative impacts of mineral dust. *Journal of Geophysical Research*, *106*(D16), 18,015–18,027.

Steltzer, H., Landry, C., Painter, T. H., Anderson, J., & Ayres, E. (2009). Biological consequences of earlier snowmelt from desert dust deposition in alpine landscapes. *Proceedings of the National Academy of Sciences, USA*, *106*(28), 11,629–11,634. www.pnas.orgcgidoi10.1073pnas.0900758106

Thind, P., Chandel, K. K., Sharma, S. K., Mandal, T. K., & Siby, J. (2019). Light-absorbing impurities in snow of the Indian Western Himalayas: Impact on snow albedo, radiative forcing, and enhanced melting. *Environmental Science and Pollution Research*, *26*(8), 7566–7578. https://doi.org/10.1007/s11356-019-04183-5

Thurston, G. D., Ito, K., & Lall, R. (2011). A source apportionment of U.S. fine particulate matter air pollution. *Atmospheric Environment*, *45*(24), 3924–3936. https://doi.org/10.1016/j.atmosenv.2011.04.070

Udall, B. (2013). Water: impacts, risks, and adaptation. In G. Garfin, A. Jardine, R. Merideth, M. Black, & S. LeRoy (Eds.), *Assessment of climate change in the southwest United States: A report prepared for the National Climate Assessment*, *A report by the Southwest Climate Alliance* (pp. 197–217). Washington, DC: Island Press.

van der Zee, C., Roberts, D. R., Rancourt, D. G., & Slomp, C. P. (2003). Nanogoethite is the dominant reactive oxyhydroxide phase in lake and marine sediments. *Geology*, *31*, 993–996.

Vassilev, S. V., & Vassilev, C. G. (1997). Geochemistry of coals, coal ashes and combustion wastes from coal-fired power stations. *Fuel Processing Technology*, *51*(1–2), 19–45. https://doi.org/10.1016/S0378-3820(96)01082-X

Wang, X. S. (2014). Mineralogical and chemical composition of magnetic fly ash fraction. *Environmental Earth Sciences*, *71*(4), 1673–1681.

Warren, S. G. (1982). Optical properties of snow. *Reviews of Geophysics and Space Physics*, *20*(1), 67–89.

Warren, S. G., & Wiscombe, W. J. (1980). A model for the spectral albedo of snow. II: Snow containing atmospheric aerosols. *Journal of Atmospheric Sciences*, *37*, 2734–2745. https://doi.org/10.1175/1520-0469(1980)037<2734:AMFTSA>2.0.CO;2

Werkenthin, M., Kluge, B., & Wessolek, G. (2014). Metals in European roadside soils and soil solution—A review. *Environmental Pollution*, *189*, 98–110. https://doi.org/10.1016/j.envpol.2014.02.025

Winkler, R., Boon, S., Zimonick, B., & Baleshta, K. (2010). Assessing the effects of post-pine beetle forest litter on snow albedo. *Hydrological Processes*, *24*(6), 803–812.

Wiscombe, W. J., & Warren, S. G. (1980). A model for the spectral albedo of snow. I: Pure snow. *Journal of Atmospheric Sciences*, *37*, 2712–2733. https://doi.org/10.1175/1520-0469(1980)037<2712:AMFTSA>2.0.CO;2

Wolf, R. E. & Adams, M. (2015). Multi-elemental analysis of aqueous geochemical samples by quadrupole inductively coupled plasma-mass spectrometry (ICP-MS). U.S. Geological Survey Open-File Report 2015–1010. https://doi.org/10.3133/ofr20151010

Wu, C., Liu, X., Lin, Z., Rahimi-Esfarjani, S. R., & Zheng Lu, Z. (2018). Impacts of absorbing aerosol deposition on snowpack and hydrologic cycle in the Rocky Mountain region based on variable-resolution CESM (VR-CESM) simulations. *Atmospheric Chemistry and Physics*, *18*(511–533), 2018. https://doi.org/10.5194/acp-18-511-2018

Wu, G., Xu, T., Zhang, X., Zhang, C., & Yan, N. (2016). The visible spectroscopy of iron oxide minerals in dust particles from ice cores on the Tibetan Plateau. *Tellus B: Chemical and Physical Meteorology*, *68*, 1. https://doi.org/10.3402/tellusb.v68.29191

Zhang, X. L., Wu, G. J., Zhang, C. L., Xu, T. L., & Zhou, Q. Q. (2015). What's the real role of iron-oxides in the optical properties of dust aerosols? *Atmospheric Chemistry and Physics*, *15*(4), 5619–5662. https://doi.org/10.5194/acpd-15-12159-2015

Zhang, Y. L., Kang, S., Cong, Z., Schmale, J., Sprenger, M., Li, C., et al. (2017). Light-absorbing impurities enhance glacier albedo reduction in the southeastern Tibetan Plateau. *Journal of Geophysical Research: Atmospheres*, *122*, 6915–6933. https://doi.org/10.1002/2016JD026397

Zhang, Y. L., Kang, S., Sprenger, M., Cong, Z., Gao, T., Li, C., et al. (2018). Black carbon and mineral dust in snow cover on the Tibetan Plateau. *The Cryosphere*, *12*, 413–431. https://doi.org/10.5194/tc-12-413-2018

Zhao, C., Hu, Z., Qian, Y., Leung, L., Huang, J., Huang, M., et al. (2014). Simulating black carbon and dust and their radiative forcing in seasonal snow: A case study over North China with field campaign measurements. *Atmospheric Chemistry and Physics*, *14*, 11,475–11,491. https://doi.org/10.5194/acp-14-11475-2014

References From the Supporting Information

Carter-Stiglitz, B., Banerjee, S. K., Gourlan, A., & Oches, E. (2006). A multi-proxy study of Argentina loess: Marine oxygen isotope stage 4 and 5 environmental record from pedogenic hematite. *Palaeogeography, Palaeoclimatology, Palaeoecology*, *239*, 45–62. https://doi.org/10.1016/j.palaeo.2006.01.008

Dunlop, D. J., & Özdemir, Ö. (1997). *Rock Magnetism: Fundamentals and Frontiers* (573 pp.). New York, London and Cambridge: Cambridge University Press.

Frandsen, C., & Mørup, S. (2005). Spin rotation in $\alpha-Fe_2O_3$ nanoparticles by interparticle interactions. *Physical Review Letters*, *94*. https://doi.org/10.1103/PhysRevLett.94.027202

Jiang, Z., Liu, Q., Dekkers, M. J., Colombo, C., Yu, Y., Barron, V., & Torrent, J. (2014). Ferro and antiferromagnetism of ultrafine grained hematite. *Geochemistry, Geophysics, Geosystems*, *15*, 2699–2712. https://doi.org/10.1002/2014GC005377

Lagroix, F., & Guyodo, Y. (2017). A new tool for separating the magnetic mineralogy of complex mineral assemblages from low temperature magnetic behavior. *Frontiers Earth Science*, *5*, 61. https://doi.org/10.3389/feart.2017.00061

Liu, Q., Yu, Y., Torrent, J., Roberts, A. P., Pan, Y., & Zhu, R. (2006). Characteristic low-temperature magnetic properties of aluminous goethite [α-(Fe, Al)OOH] explained. *Journal of Geophysical Research*, *111*, B12S34. https://doi.org/10.1029/2006JB004560

Maher, B. A., Karloukovski, V. V., & Mutch, T. J. (2004). High-field remanence properties of synthetic and natural submicrometre hematites and goethites: Significance for environmental contexts. *Earth and Planetary Science Letters*, *226*, 491–505. https://doi.org/10.1016/j.epsl.2004.05.042

Morris, R. V., Golden, D. C., Bell, J. F., Shelfer, T. D., Scheinost, A. C., Hinman, N. W., et al. (2000). Mineralogy, composition, and alteration of Mars Pathfinder rocks and soils: Evidence from multispectral, elemental, and magnetic data on terrestrial analogue, SNC meteorite, and pathfinder samples. *Journal of Geophysical Research*, *105*(E1), 1757–1817. https://doi.org/10.1029/1999JE001059

Özdemir, Ö., & Dunlop, D. J. (2006). Magnetic memory and coupling between spin-canted and defect magnetism in hematite. *Journal of Geophysical Research*, *111*, B12S03. https://doi.org/10.1029/2006JB004555

Özdemir, Ö., Dunlop, D. J., & Berquó, T. S. (2008). Morin transition in hematite: Size dependence and thermal hysteresis. *Geochemistry, Geophysics, Geosystems*, *9*, Q10Z01. https://doi.org/10.1029/2008GC002110

Rochette, P., & Fillion, G. (1989). Field and temperature behavior of remanence in synthetic goethite: Paleomagnetic implications. *Geophysical Research Letters*, *16*, 851–854.

Rochette, P., Mathe, P. E., Esteban, L., Rakoto, H., Bouchez, J. L., Liu, Q., & Torrent, J. (2005). Non-saturation of the defect moment of goehtite and fine-grained hematite up to 57 teslas. *Geophysical Research Letters*, *32*, L2239. https://doi.org/10.1029/2005GL024196

Vandenberghe, R. E., Van San, E., De Grave, E., & DaCosta, G. M. (2001). About the Morin transition in hematite in relation with particle size and aluminum substitution. *Czechoslovak Journal of Physics*, *51*, 663–675.